DEFECTS IN ZINC OXIDE NANOCRYSTALS

By

SAMUEL TESFAI TEKLEMICHAEL

A dissertation submitted in partial fulfillment of
the requirements for the degree of

DOCTOR OF PHILOSOPHY

WASHINGTON STATE UNIVERSITY
Department of Physics and Astronomy

AUGUST 2012

To the Faculty of Washington State University:

The members of the Committee appointed to examine the dissertation of SAMUEL TESFAI TEKLEMICHAEL find it satisfactory and recommend that it be accepted.

Matthew D. McCluskey, Ph.D., Chair

Gary S. Collins, Ph.D.

Yi Gu, Ph.D.

ACKNOWLEDGEMENTS

First and foremost, I am truly indebted and thankful to my advisor, Prof. Matthew McCluskey, for his support, patience and guidance he showed me throughout my research. His unsurpassed knowledge of the subject, wisdom and ability to advice in a unique and simple way has amazingly inspired me. My thanks also go to Prof. Jeanne McHale for listening and answering my questions during her busy schedules. I would also like to thank my dissertation committee, Prof. Yi Gu and Prof. Gary Collins for their invaluable and helpful suggestions.

I am obliged to the two of former graduate students in our group: Dr. Win Maw Oo and Dr. Slade Jokela. Win has taught me how to synthesize ZnO nanoparticles and helped me in introducing our FTIR spectrometer and other lab instruments. Slade has also wonderfully assisted me in various ways during my experimental works.

I owe sincere and earnest thankfulness to all members of the Department of Physics and Astronomy. I am also grateful to my fellow graduate students Ann Tarun, Narendra Parmar, Enam Kahn, Shiva Ramini and Ranga Dias for their wonderful Physics discussions. I especially thank Dr. Natnael Embaye, my cousin and a former graduate student of Prof. Kuzyk, for his encouragement and following every step of my research progress.

I would like to extend my gratitude to members of the Pacific Northwest National Laboratory (PNNL): Dr. Eric Walter, Dr. David Hoyt and Dr. Chongming Wang for their assistance to conduct my experiment at Environmental Molecular Science Laboratory (EMSL).

Last, but by no means least, my deepest thanks go to my parents, brothers and sisters, without whose love, support and encouragement, I would not have completed this dissertation.

DEFECTS IN ZINC OXIDE NANOCRYSTALS

Abstract

by Samuel Tesfai Teklemichael, Ph.D.
Washington State University
August, 2012

Chair: Matthew D. McCluskey

Defects in ZnO nanocrystals were investigated. While ZnO has potential for optoelectronic applications, the lack reliable *p*-type doping remains a major challenge. We provide evidence that ZnO nanocrystals contain uncompensated acceptors. IR absorption peaks at liquid-helium temperatures suggest a hydrogenic acceptor with a hole binding energy of 0.4 - 0.5 eV. Electron paramagnetic resonance (EPR) measurements in the dark showed a resonance at $g = 2.003$, characteristic of acceptors that involve a zinc vacancy. An EPR resonance due to vacancy hydrogen complexes was observed after exposure to light.

Using infrared (IR) and photoluminescence (PL) spectroscopy, we have developed a unified model for the acceptor and intragap surface states of ZnO nanocrystals. A PL peak was observed at 2.97 eV, in agreement with the acceptor level observed in the IR. The temperature dependence of the IR absorption peaks, which correspond to a hole binding energy of 0.46 eV, showed an ionization activation energy of only 0.08 eV. This activation energy is attributed to thermal excitation of the hole to surface states 0.38 eV above the valence band maximum.

Therefore, while the acceptor is deep with respect to the bulk valence band, it is shallow with respect to surface states. A strong red PL emission centered at 1.84 eV, with an excitation onset of 3.0 eV, is attributed to surface recombination.

IR absorption peaks at liquid-helium temperatures, which correspond to electronic transitions of the acceptor, disappeared after exposure to formic acid (HCOOH) vapor. This observation is consistent with electrical compensation of the acceptor by the formate ion. The energy level of the formate ion is estimated to be ~ 0.9 eV above the valence-band maximum. Room temperature IR measurements show that the formate species are adsorbed on the surface of ZnO nanocrystals. A broad PL peak centered at 3.2 eV, for samples exposed to HCOOH, is attributed to an exciton bound to a formate species.

High field EPR measurements of ZnO nanocrystals showed new resonances, in addition to the previously observed line at $g = 2.003$. We propose a model of two systems with an axial center of $g_{\perp} = 2.003274$ and $g_{//} = 2.007471$ along with an isotropic center at $g = 2.005254$. Samples exposed to HCOOH did not show a complete disappearance of the EPR resonances. Instead, a decrease in intensity is observed.

TABLE OF CONTENTS

List of figures

List of tables

This dissertation is dedicated to my wonderful, loving and caring parents, Tesfai and Mebrat.

Chapter 1 Introduction

1.1 Oxide semiconductors

1.1.1 Background

Oxide semiconductors such as TiO_2, ZnO, SnO_2 and In_2O_3 have stimulated tremendous interest in the past decade. They are attractive for numerous applications including gas sensors, transparent conducting films, catalysis, energy storage and conversion, and optoelectronics [1-3]. Their nanostructures, in particular, have been widely investigated as gas sensors due to their small dimensions, low cost, and high compatibility with microelectronic processing [4]. Owing to their large surface-to-volume ratio and a Debye length comparable to the small size, they demonstrate superior sensitivity to surface chemical processes. Yamazoe [1] showed that the sensor performance is strongly improved when the size of the nanocrystals is smaller than twice the Debye length (~ 3 nm for SnO_2). The catalysis effect is another interesting field where high surface area and size-dependent properties play significant roles. These important features have led researchers to investigate nanostructured materials with a wide variety of experimental probes. Size effect (quantum confinement), for instance, is well studied using Raman scattering [5, 6].

The following sections will summarize the general properties and practical applications of several wide-band-gap oxide semiconductors. I will then give a more detailed discussion on ZnO nanostructures, the subject of this research.

1.2 Titania (TiO_2)

Titania (TiO_2) is a wide band gap semiconductor that has been actively investigated due to its range of applications. It exhibits two main crystalline phases, anatase (suitable for catalysis and supports) [7] and rutile (used for optoelectronic purposes) [8]. Recent interest in TiO_2 nanocrystals is fueled by its key role in the injection process in a photochemical solar cell with high conversion efficiency. By using semiconductor films consisting of nanometer-sized TiO_2 particles, O'Regan and Grätzel [9] improved the efficiency and stability of the solar cell. Studying the adsorption of carboxylic acids, for the purpose of TiO_2-based dye-sensitized electrochemical devices, is also important [10]. Fourier transform infrared spectroscopy (FTIR) is commonly used for studying the adsorption properties of organic species such as formic acid, where formate signatures can easily be detected by IR [11].

1.3 Tin oxide (SnO_2)

Tin oxide (SnO_2) is another interesting semiconducting oxide material. Its large band gap (3.6 eV at room temperature), high transparency in the visible region and high conductivity make the material ideal for transparent conductive electrode on devices such as solar cells [12]. SnO_2 nanoparticles have also been extensively used as a sensor material, owing to its high sensitivity to low gas concentrations [1]. Using photoluminescence (PL) experiments, Faglia *et al.* [13] reported that the visible emission of SnO_2 nanobelts is quenched reversibly after exposing to NO_2 at ppm levels, indicating the strong sensitivity of SnO_2. Moreover, Lu *et al.* [14] showed that the sensitivity of nano-sized SnO_2 powder, grown by sol-gel method, increased with the reduction of particle size. They indicated that the response to 500 ppm CO increases drastically for particles with diameter smaller than 10 nm. This size effect advantage of sensing is expected to be the same in other oxide nanostructured materials.

1.4 Zinc oxide (ZnO)

Zinc oxide (ZnO) is one of the most prominent and widely studied semiconductors in the metal oxide family. Its wide band gap (3.37 eV) and large exciton binding energy (60 meV) [15] ensure efficient exciton ultraviolet (UV) emission at room temperatures [16]. ZnO has been used as a buffer layer for growth of GaN-based devices [17], as a transparent conductive oxide [18] in solar cells [19], and as a transducer for micro electrical-mechanical systems [20]. ZnO nanostructures offer promising applications in nanotechnologies and devices. Ferromagnetic quantum dots could also be used in high density storage devices [21].

ZnO forms in the hexagonal wurtzite crystal structure (Fig. 1.1) with lattice parameters $a = 0.32495$ nm and $c = 0.52069$ nm [22]. The ratio of $c/a = 1.602$ is close to the ideal hexagonal structure, 1.633. The Zn atoms form a tetrahedral coordination with four O atoms, where the Zn d-orbitals hybridize with the p-orbitals of O atoms.

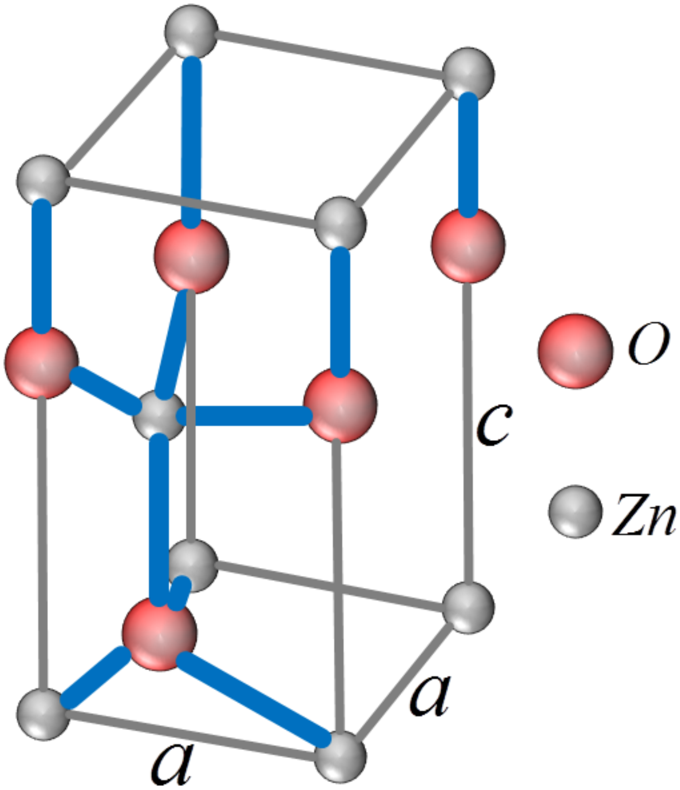

Figure 1.1: Hexagonal wurtzite ZnO.

1.4.1 Electrical properties

As-grown, ZnO is typically *n*-type in bulk and thin films [23, 24], which has long been ascribed to native defects such as O vacancies or Zn interstitials [24-27]. However, theoretical calculations show that the O vacancy is a deep donor [28] and cannot contribute to *n*-type conductivity. Electron paramagnetic resonance (EPR) results also showed that O vacancy signals could be detected only after high-energy electron irradiation [29, 30]. Zn interstitials are shallow donors but are not stable at room temperature as pointed out by theory [28] and experiment [31, 32]. Given that native defects cannot explain *n*-type conductivity, impurities are likely play the largest role. Recently it was shown that H and the group-III elements are present in bulk ZnO crystals and act as donors [33]. First-principles calculations have shown that H is a shallow donor in ZnO [34], attracting attention to investigate its role in the electronic properties of ZnO. The shallow donor nature of H in ZnO was confirmed experimentally using muon spin rotation (μSR) [35] and electron nuclear double resonance (ENDOR) [36] techniques.

Reliable *p*-type ZnO remains controversial despite numerous reports in the literature. Proposed acceptor dopants include substitution of N on O sites [37], and group-I elements such as Li [38] and group-IB elements such as Cu [39] substituting on Zn sites. However, experimental studies have shown that Li and Cu are deep acceptors [33]. Calculations have suggested that N, once thought to be a hydrogenic acceptor, is actually a deep acceptor with significant lattice relaxation [40, 41]. Recent experimental results are consistent with this deep-acceptor model [42].

1.4.2 Optical properties

The optical properties of ZnO depend on both intrinsic and extrinsic effects. At the zone center, the conduction band is mainly *s* like and the valence band is *p* like, splitting into three levels (*A*, *B*, and *C*) due to spin-orbit and crystal-field splitting. PL measurements indicated that the *A* free exciton has a binding energy of 60 meV [43], resulting in efficient excitonic emission that persists at room temperature [16]. Room-temperature UV lasing has been demonstrated in ZnO nanowires. Using PL experiments, Huang *et al.* [44] observed the lasing action in nanowires via the evolution of the emission spectra with increasing pump power. ZnO has also strong non-linear optical applications, exhibiting second-order nonlinear optical behavior [45].

The green luminescence band centered around 2.4 eV is the most commonly seen defect emission in ZnO. Its attribution remains highly controversial. Early studies showed that Cu impurities, common trace impurities in ZnO, cause green emission [46]. Later, native defects such as O vacancies [47] and Zn vacancies [48] were proposed as a main source. Theoretical calculations [28] showed that the transition between the conduction band (or a shallow donor) and the Zn vacancy acceptor level could give rise to a PL around 2.5 eV.

The primary focus of this work is to investigate the defect properties of ZnO nanocrystals, with an emphasis on acceptor type defects.

1.4.3 Synthesis of ZnO nanostructures

Various methods have been adopted for synthesizing ZnO nanostructures, including sol-gel method, thermal decomposition and colloidal synthesis [49-53]. Different precursors such as zinc acetate, zinc nitrate, or zinc carbonate can be used in growing ZnO nanocrystals. During the growth process, reaction of Zn salts with hydroxide ions is commonly involved [54]. In this process, temperature, water content, and solvents are important growth parameters. The key challenge in synthesizing ZnO nanocrystals is controlling of size uniformity and chemical stability of the nanoparticles. Polymers such as polyvinyl pyrrolidone (PVP) can be used as capping molecules to stabilize ZnO nanoparticles [55].

High-quality ZnO nanoparticles, with low cost, can be achieved by solid-state pyrolytic reaction method as developed by Wang *et al.* [56]. In this method, zinc acetate and sodium hydrogen carbonate were reacted at the reaction temperature. The zinc acetate forms ZnO nanoparticles by a thermal decomposition process and the byproduct, sodium acetate, is washed away with water. They demonstrated that the particle size is controlled by the pyrolytic temperature. This approach of synthesizing ZnO nanocrystals has been used in this work.

1.5 Outline of the dissertation

Chapter 2 describes theoretical background related to this work. In chapter 3, the experimental techniques used for this work are presented. Chapter 4 discusses the presence of acceptor related defects in ZnO nanocrystals, observed by IR spectroscopy. A unified model that explains the presence of acceptor and surface states in ZnO nanocrystals is presented in Chapter 5. Chapter 6 reports compensation of acceptors in ZnO nanocrystals by adsorption of formic acid (HCOOH). A high field electron paramagnetic resonance (EPR) study of ZnO nanocrystals is presented in Chapter 7. In Chapter 8 I will discuss on IR studies of copper doped ZnO nanoparticles.

References

[1]. N. Yamazoe, Sens. Actuators B **5,** 7 (1991).

[2]. D. S. Ginley and C. Bright, Mater. Res. Soc. Bull. **25,** 15 (2000).

[3]. J. L. G. Fierro, Metal Oxides: *Chemistry and Applications*, (CRS Press, Boca Raton, FL, 2006).

[4]. G. Eranna, *Metal Oxide Nanostructures As Gas Sensing Devices*, (CRS Press: Boca Raton, FL, 2012).

[5]. K. A. Alim, V. A. Fonoberov, and A. A. Balandin, Appl. Phys. Lett. **86,** 053103 (2005).

[6]. V. Swamy, B. C. Muddle, and Q. Dai, Appl. Phys. Lett. **89,** 163118.

[7]. K. Foger, and J. R. Anderson, Appl. Catal. **23,** 139 (1986).

[8]. F. Zhang, Z. Zheng, X. Ding, Y. Mao, Y. Chen, Z. Zhou, S. Yang and X. Liu, J. Vac. Sci. Technol., A **15,** 1824 (1997).

[9]. B. O'Regan and M. Grätzel, Nature **353,** 737 (1991).

[10]. Q.-L. Zhang, L.-C. Du, Y.-X. Weng, L. Wang, H.-Y. Chen and J.-Q. Li, J. Phys. Chem. B **108,** 15077 (2004).

[11]. L. Ojamäe, C. Aulin, H. Pedersen and P.-O. Käll, J. Colloid Interface Sci. **296,** 71 (2006).

[12]. O. P. Agnihotri, M. T. Mohammad, A. K. Abass, and K. I. Arshak, Solid State Commun. **47,** 195 (1983).

[13]. G. Faglia, C. Baratto, G. Sberveglieri, M. Zha, and A. Zappettini, Appl. Phys. Lett. **86,** 011923 (2005).

[14]. F. Lu, Y. Liu, M. Dong, and X. Wang, Sens. Actuat. B **66,** 225 (2000).

[15]. Y. Chen, D. M. Bagnall, H.-J. Koh, K.-T. Park, K. Hiraga, Z.-Q. Zhu, and T. Yao, J. Appl. Phys. **84**, 3912 (1998).

[16]. D.J. Gargas, H. Gao, H. Wang, and P. Yang, Nano Letters **11**, 3792 (2011).

[17]. T. Detchprohm, K. Hiramatsu, H. Amano, and I. Akasaki, Appl. Phys. Lett**.** **61**, 2688 (1992).

[18]. T. Minami, MRS Bull. **25,** 38 (2000).

[19]. M. A. Martinez, J. Herrero and M. T. Gutierrėz, Solar Energy Materials and Solar Cells **45,** 75 (1997).

[20]. P. M. Martin, M. S. Good, J. W. Johnston, G. J. Posakony, L. J. Bond, and S. L. Crawford, Thin Solid Films **379,** 253 (2000).

[21]. S. J. Pearton, C. R. Abernathy, M. E. Overberg, G. T. Thaler, D. P. Norton, N. Theodoropoulou, A. F. Hebard, Y. D. Park, F. Ren, J. Kim, and L. A. Boatner, J. Appl. Phys. **93,** 1 (2003).

[22]. S. J. Pearton, D. P. Norton, K. Ip, Y. W. Heo, and T. Steiner, Progress in Materials Science **50,** 293 (2005).

[23]. D. C. Look, D. C. Reynolds, J. R. Sizelove, R. L. Jones, C. W. Litton, G. Cantwell, and W. C. Harsch, Solid State Commun. **105,** 399 (1998).

[24]. D. C. Look, Mater. Sci. Eng. B **80,** 383 (2001).

[25]. F. A. Kröger, *The Chemistry of Imperfect Crystals*, (North Holland Publishing, Amsterdam 1974).

[26]. D. C. Look, J. W. Hemsky, and J. R. Sizelove, Phys. Rev. Lett. **82,** 2552 (1999).

[27]. G. W. Tomlins, J. L. Routbort, and T. O. Mason, J. Appl. Phys. Rev. **87,** 117 (2000).

[28]. A. Janotti and C. G. Van de Walle, Phys. Rev. B **76,** 165202 (2007).

[29]. L. S. Vlasenko and G. D. Watkins, Phys. Rev. B **71,** 125210 (2005).

[30]. S. M. Evans, N. C. Giles, L. E. Halliburton, and L. A. Kappers, J. Appl. Phys. **103,** 043710 (2008).

[31]. L. S. Vlasenko and G. D. Watkins, Phys. Rev. B **72,** 035203 (2005).

[32]. W. E. Carlos, E. R. Glasier, and D. C. Look, Physica B **308-310,** 976 (2001).

[33]. M. D. McCluskey and S. J. Jokela, J. Appl. Phys. **106,** 071101 (2009).

[34]. C. G. Van de Walle, Phys. Rev. Lett. **85,** 1012 (2000).

[35]. S. F. J. Cox, E. A. Davis, S. P. Cottrell, P. J. C. King, J. S. Lord, J. M. Gil, H. V. Alberto, R. C. Vilao, J. P. Duarte, N. A. de Campos, A. Weidinger, R. L. Lichti, and S. J. C. Irvine, Phys. Rev. Lett. **86,** 2601 (2001).

[36]. D. M. Hofmann, A. Hofstaetter, F. Leiter, H. J. Zhou, F. Henecker, B. K. Meyer, S. B. Orlinskii, J. Schmidt, and P. G. Baranov, Phys. Rev. Lett. **88,** 045504 (2002).

[37]. C. H. Park, S. B. Zhang, and S.-H. Wei, Phys. Rev. B **66,** 073202 (2002).

[38]. O. F. Schirmer, J. Phys. Chem. Solids **29**, 1407 (1968).

[39]. Y. Kanai, Jpn. J. Appl. Phys., Part 1 **30,** 703 (1991).

[40]. J. L. Lyons, A. Janotti, and C. G. Van de Walle, Appl. Phys. Lett. **95**, 252105 (2009).

[41]. S. Lany and A. Zunger, Phys. Rev. B **81,** 205209 (2010).

[42]. M. C. Tarun, M. Z. Iqbal, and M. D. McCluskey, AIP Advances **1,** 022105 (2011).

[43]. A. Teke, Ü. Özgür, S. Doğan, X. Gu, H. Morkoç, B. Nemeth, J. Nause, and H. O. Everitt, Phys. Rev. B **70,** 195207 (2004).

[44]. M. H. Huang, S. Mao, H. Feick, H. Yan, Y. Wu, H. Kind, E. Weber, R. Russo, and P. Yang, Science **292,** 1897 (2001).

[45]. K. Ozga, T. Kawaharamura, A. Ali Umar, M. Oyama, K. Nouneh, A. Slezak, S. Fujita, M. Piasecki, A. H. Reshak, and I. V. Kityk, Nanotechnology **19,** 185709 (2008).

[46]. R. Dingle, Phys. Rev. Lett. **23,** 579 (1969).

[47]. K. Vanheusden, W. L. Warren, C. H. Seager, D. R. Tallant, J. A. Voigt, and B. E. Gnade, J. Appl. Phys. **79,** 7983 (1996).

[48]. T. Sekiguchi, N. Ohashi, and Y. Terada, Jpn. J. Appl. Phys., Part 2 **36,** L289 (1997).

[49]. L. Spanhel, M. A. Anderson, J. Am. Chem. Soc. **113,** 2826 (1991).

[50]. S. Chu, T. Yan, S. Chen, J. Mater. Sci. Lett. **19,** 349 (2000).

[51]. B. Chiou, Y. Tsai, J. Duh, J. Mater. Sci. Lett. **7,** 785 (1988).

[52]. N. Audebrand, J. Auffrédic, D. Louër, Chem. Mater. **10,** 2450 (1998).

[53]. E. Wong, J. Bonevich, P. Searson, J. Phys. Chem. B. **102,** 7770 (1998).

[54]. Z. Hu, G. Oskam, and P. C. Searson, J. Colloid Interface Sci. **263,** 454 (2003).

[55]. L. Guo, S. Yang, C. Yang, P. Yu, J. Wang, W. Ge, and G. K. L. Wong, Appl. Phys. Lett., **76,** 2901 (2000).

[56]. Z. Wang, H. Zhang, L. Zhang, J. Yuan, S. Yan, and C. Wang, Nanotechnology **14,** 11 (2003).

Chapter 2 Theory

In this chapter, I discuss the theoretical background and explanations for the work presented in chapter 4. The section follows the definitions, treatment and framework given in the books by Cotton [1] and McCluskey and Haller [2].

2.1 Group theory

A group is a collection of elements which are interrelated according to certain rules [1]. For the set of elements to form a mathematical group, the following rules must be obeyed.

1. The product of any two elements, A and B, in the group and the square of each element must be an element in the group: $AB = C$ where C is also an element in the group. The term product does not necessarily mean arithmetic multiplication. It can be any combination of operations.
2. An element in the group, called the identity E, must commute with all others and leave them unchanged: $EX = XE = X$.
3. The associative law, $A(BC) = (AB)C$, of multiplication must hold.
4. Every element must have a reciprocal, which is also an element of the group. The element R is the reciprocal of S if $RS = SR = E$. Moreover, E is its own reciprocal.

The following symmetry operations can be performed to describe a particular molecule.

- Inversion (***i***): If a molecule can be brought into an equivalent configuration by changing the (x, y, z) coordinates into $(-x, -y, -z)$, then it has an inversion symmetry.

- Proper rotation (**C_n**): A molecule with proper rotation symmetry can be brought to an equivalent configuration if rotated, by an angle $2\pi/n$, through an axis of rotation. where n denotes the order of the axis. When an electron is considered, due to the spin, a rotation by an $4\pi/n$ forms a set of rotations (double groups).
- Improper rotation (**S_n**): A symmetry operation involving a proper rotation followed by a reflection through a plane perpendicular to the rotation axis.
- Reflection (**σ**): Reflection in a mirror plane can leave a molecule invariant. Reflection in the mirror plane can be denoted either by $\boldsymbol{\sigma}_{\mathbf{v}}$ or $\boldsymbol{\sigma}_{\mathbf{h}}$, depending on whether the plane passes through the main axis of rotation or is perpendicular to it, respectively.

2.1.1 Examples of point groups

Water (H_2O)

The water molecule has a planar structure with a H-O-H angle of 105° (Fig. 2.1). The following symmetry operations leave the molecule invariant.

- A twofold rotation (180°) axis passing through O atom and bisecting a line between the two H atoms.
- Two vertical planes, one of which is the molecular plane.

Therefore the point group of H_2O molecule is C_{2v}.

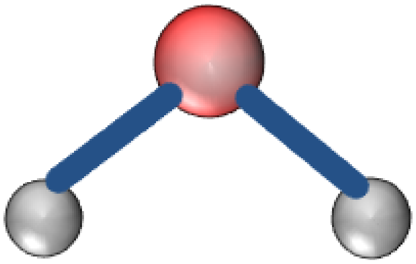

Figure 2.1: Water molecule.

Silicon (Si) with impurities

An example of a defect with a point group of C_{3v} will be presented. Fig. 2.2 shows a B-H complex in Si which has the following symmetry operations.

- Two threefold rotations (120° and 240°) about the z-axis.
- There are three vertical planes, one passing through each Si atoms. Therefore the point group belongs to C_{3v}.

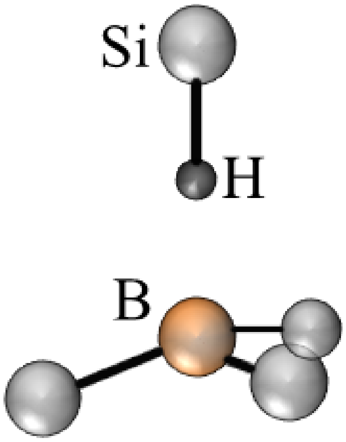

Figure 2.2: B-H complex in Si, an example of C_{3v} symmetry.

2.1.2 Theoretical background

The symmetry operations discussed in section 2.1.1 can be described by a matrix T, reducing the group theory to the algebra of matrices. The set of matrices, each corresponding to a single operation in the group, can define a *representation* of the group, denoted by Γ. If there are two sets of matrices {A} and {B} which form representations of the group, then these representations are said to be equivalent if they obey the rule:

$$\{B\} = \mathrm{C}^{-1}\{\mathrm{A}\}\mathrm{C}. \tag{2.1}$$

Eq. (2.1) states that there is an invertible matrix C such that for any matrix from set {A} there is a matrix in set {B} which can be obtained by a unitary transformation. It is possible that a set of matrices can be transformed into a new one so that all of the new ones can be taken apart in the same way to give two or more representations of smaller dimensions. Such representation that can be simultaneously block-factored is called a *reducible* representation. Otherwise it is called *irreducible*. It is the irreducible representations of the group which are of interest to us.

The character $\chi(R)$ of a given operation R is defined as the trace of a matrix of a given operation. The character of the representation is given by the set of all characters for a particular representation. A group can be described fully by a *character table* in the case of an irreducible representation of a point group. The properties of such group representation and their characters can be derived from one basic theorem, *the great orthogonality theorem*, which can be stated as follows. The proof can be found elsewhere [3].

$$\sum_R [\Gamma_i(R)_{mn}][\Gamma_j(R)_{m'n'}]^* = \frac{h}{\sqrt{l_i l_j}}\delta_{ij}\delta_{mm'}\delta_{nn'}, \tag{2.2}$$

where $\Gamma_i(R)_{mn}$ and $\Gamma_j(R)_{mn}$ are the *i*th and *j*th irreducible representation of an operation *R* with dimensions of l_i and l_j, respectively. *h* is the order of the group. By applying this theorem, reducible representations of a given group can be written as a sum of irreducible representations, which has pivotal applications in electronic and vibrational properties of molecules.

2.2 Electronic properties of defects

In this section I will discuss the electronic properties of defects, with an emphasis on hydrogenic impurities, relevant to the work in chapter 4.

2.2.1 Hydrogenic model

Defects in semiconductor crystals can introduce energy levels inside the band gap. The energy levels can be referred as either *shallow* or *deep*, depending on the binding energy they acquire. Donor (acceptor) levels that are close to the conduction band minimum (valence band maximum) are called shallow. They form a low binding energy in which the electron (hole) is given up to the conduction (valence) band at moderate temperature. Shallow donors (acceptors) are called hydrogenic because they can be described as an electron (hole) orbiting an ion, analogous to the hydrogen atom embedded in a homogenous medium with a relative dielectric constant and an electron/hole mass that corresponds the effective mass of the particular band extremum. For the derivation of the energy of a hydrogenic model, I will follow the treatment provided in the book by McCluskey and Haller [2].

Consider an electron orbiting a positively charged phosphorous donor in a silicon crystal as shown in Fig. 2.3. The Coulomb force of attraction between the electron and the phosphorous ion is given by

$$F = \frac{1}{4\pi\varepsilon\varepsilon_0}\frac{e^2}{r^2}, \tag{2.3}$$

where r is the radius of the orbit. The orbiting electron experiences a repulsive centrifugal force which is given by Newton's second law of motion,

$$F = m^* a = m^* v^2 / r, \tag{2.4}$$

where m^* and v are the mass and speed of the electron, respectively. Two important conditions are considered in the Bohr model of a hydrogen atom, (1) the balance between the Coulomb attractive and repulsive centrifugal forces and (2) the quantization of the angular momentum L of the electron moving in a circular orbit. These two conditions can be mathematically written as

$$\frac{1}{4\pi\varepsilon\varepsilon_0}\frac{e^2}{r^2} = \frac{m^* v^2}{r}, \tag{2.5}$$

$$L = m^* v r = \hbar n, \tag{2.6}$$

where n is a positive integer (n= 1, 2, 3…). From Eqs. (2.5) and (2.6), the speed and the radius of the electron can be solved as

$$v = \frac{e^2}{4\pi\varepsilon\varepsilon_0 \hbar n}. \tag{2.7}$$

$$r = \frac{4\pi\hbar^2\varepsilon\varepsilon_0}{e^2 m^*} n^2. \tag{2.8}$$

The radius of the orbit in the ground state n=1 (the *donor Bohr radius*) which measures the extent of the bound-state wave functions of the electron, is given by

$$r_0 = (0.53\text{Å})\frac{\varepsilon}{m^* / m}. \tag{2.9}$$

The potential energy of the electron in a Coulomb potential is given by

$$E_P = -\frac{1}{4\pi\varepsilon\varepsilon_0}\frac{e^2}{r}. \tag{2.10}$$

Inserting the radius of the orbit from Eq. (2.8) into Eq. (2.10), the potential energy of the electron will be

$$E_P = -\frac{m^* e^4}{(4\pi\varepsilon\varepsilon_0\hbar)^2}\frac{1}{n^2}. \tag{2.11}$$

Furthermore, using the speed and the radius obtained in Eqs. (2.7) and (2.8), respectively, the kinetic energy E_K of the electron can be calculated as

$$E_K = \frac{1}{2}\frac{m^* e^4}{(4\pi\varepsilon\varepsilon_0\hbar)^2}\frac{1}{n^2}. \tag{2.12}$$

The total energy E of the electron is given by the sum of the electron's kinetic and potential energies, written by

$$E = E_K + E_P = -\frac{1}{2}\frac{m^* e^4}{(4\pi\varepsilon\varepsilon_0\hbar)^2}\frac{1}{n^2}. \tag{2.13}$$

From Eq. (2.13) we notice that the quantization of the angular momentum leads to the quantization of its total energy. For large values of n, the total energy becomes less negative and approaches zero as n approaches to infinity. The donor binding energy E_d is the energy required to bring the electron from the ground state $(n = 1)$ to the conduction-band minimum, given by

$$E_d = \frac{1}{2}\frac{m^* e^4}{(4\pi\varepsilon\varepsilon_0\hbar)^2} = (13.6\ \text{eV})\left(\frac{m^*}{m}\right)\left(\frac{1}{\varepsilon^2}\right). \tag{2.14}$$

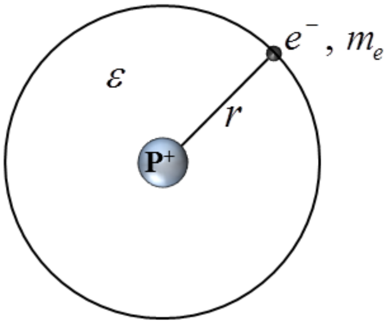

Figure 2.3: Bohr model for the phosphorus donor in silicon, showing an electron orbiting the positively charged phosphorus ion.

The hydrogenic model is valid for acceptors as well. Substitution of a boron atom in a silicon atom creates a deficiency of a valence electron. We can think of an acceptor atom possessing an *extra hole* orbiting around the negatively charged boron acceptor (Fig. 2.4). Equation (2.14) can be used to calculate the acceptor binding energy E_a, where m^* is the hole effective mass. IR light can excite the hole into higher-energy orbits, resulting in spectral lines similar to the 1 *s*-to-2 *p* transitions in hydrogen.

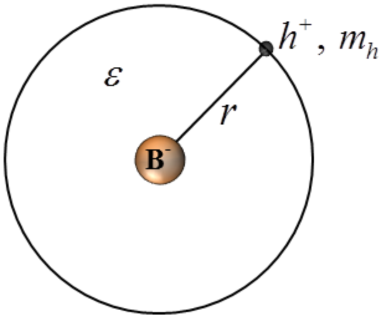

Figure 2.4: Bohr model for the boron acceptor in silicon, showing a hole orbiting the negatively charged boron ion.

The electron and hole binding energies in Si ($\varepsilon = 11.7$) are $E_d \approx 33$ meV and $E_a \approx 75$ meV, respectively. The electrons or holes of shallow local impurities are strongly *delocalized*. Their wavefuctions are extended over a large volume compared to the space taken up by each host atom. Owing to this averaging over many host atoms, the crystal can therefore be approximated as a continuous medium with an average dielectric constant ε.

2.2.2 Helium-like systems

As single donors and acceptors are solid-state analogs of the H atom, one would therefore expect double donors and acceptors to behave as He-like systems. In this section, we review the properties of a He atom, where the solution to the two-particle Schrödinger equation can be approximated using perturbation theory or the variational method. The Hamiltonian of the system is given by:

$$H = \frac{\mathbf{P}_1^2}{2m} + \frac{\mathbf{P}_2^2}{2m} - \frac{2e^2}{r_1} - \frac{2e^2}{r_2} + \frac{e^2}{r_{12}}, \tag{2.15}$$

where $r_{12} = |\mathbf{r_1} - \mathbf{r_2}|, r_1 = |\mathbf{r_1}|, r_2 = |\mathbf{r_2}|$, $\mathbf{r}$ and $\mathbf{P}$ are the positions and momenta of the two electrons, respectively. The last term is the interaction potential. In a neutral state, the interaction between the two bound electrons results in mutual screening of the nuclear charge. In this case, the spin and orbital degrees of freedom may be separated. The Pauli principle requires the total state to be antisymmetric under an exchange of particles. For the ground state configuration, $(1s)^2$, only the spin singlet state (S=0) is allowed, since the space function is necessarily symmetric. The calculated ground state energy is in better agreement with the experimental value using variational method with Z (Z_{eff}) as a variational parameter [5]. In this method, one can guess that the ground state wave function of a hydrogen atom is a trial function of the form:

$$\langle \mathbf{r} | 0 \rangle \sim e^{-r/a}, \tag{2.16}$$

where $a = \dfrac{a_0}{Z_{eff}}$ is regarded as the adjustable parameter in the trial function, a_0 and Z_{eff} are the Bohr radius and effective nuclear charge respectively. The normalized trial function for the two electrons therefore would be:

$$\langle \mathbf{r_1}, \mathbf{r_2} | 0 \rangle = \left(\frac{Z_{eff}^3}{\pi a_0^3} \right) e^{-Z_{eff}(r_1 + r_2)/a_0}. \tag{2.17}$$

From Eq. (2.15), it can be obtained that,

$$\bar{H} = \left\langle 0 \middle| \frac{\mathbf{p_1^2}}{2m} + \frac{\mathbf{P_2^2}}{2m} \middle| 0 \right\rangle - \left\langle 0 \middle| \frac{Ze^2}{r_1} + \frac{Ze^2}{r_2} \middle| 0 \right\rangle + \left\langle 0 \middle| \frac{e^2}{r_{12}} \middle| 0 \right\rangle \tag{2.18}$$

$$= \left(2\frac{Z_{eff}^2}{2} - 2ZZ_{eff} + \frac{5}{8} Z_{eff} \right) \left(\frac{e^2}{a_0} \right). \tag{2.19}$$

The energy is minimized for $Z_{eff} = 1.6875$. This value is smaller than 2, since the nuclear charge of 2e at the origin is screened by the negatively charged cloud of the other electron (Fig. 2.5). This gives a calculated energy ($E_{cal} = -77.5$ eV) which is very close to the experimental value ($E_{\exp} = -78.8$ eV).

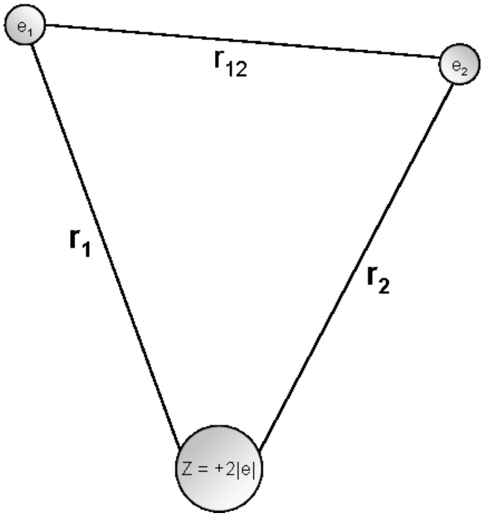

Figure 2.5: Schematic diagram of a He atom.

The energies of the excited states of neutral He (He^0) may be determined to first approximation within the Hartree-Fock, or central-field approximation. The potential felt by the electron in the excited state is effectively screened by the tightly bound (1*s*) electron. There is small overlap between (1*s*) and (2*p*) orbitals. Following the approach given by Sakurai, the energies of the state (1*s*)(*nl*) can be written as:

$$E = E_{100} + E_{nlm} + \Delta E, \tag{2.20}$$

where ΔE is calculated by evaluating the expectation value of $\frac{e^2}{r_{12}}$. From first-order perturbation theory, this is given by:

$$\left\langle \frac{e^2}{r_{12}} \right\rangle = I \pm J, \tag{2.21}$$

where I and J are known as direct and exchange integrals, respectively, and the upper (lower) sign indicates singlet (triplet) states. Their values are given by:

$$I = \int d^3 r_1 \int d^3 r_2 \left|\psi_{100}(\mathbf{r}_1)\right|^2 \left|\psi_{nlm}(\mathbf{r_2})\right|^2 \frac{e^2}{r_{12}}. \tag{2.22}$$

$$J = \int d^3 r_1 \int d^3 r_2 \psi_{100}(\mathbf{r}_1) \psi_{nlm}(\mathbf{r_2}) \frac{e^2}{r_{12}} \psi^*_{100}(\mathbf{r_2}) \psi^*_{nlm}(\mathbf{r_1}). \tag{2.23}$$

The above expressions qualitatively explain the relative positions of the singlet and triplet states. For the singlet term, the orbital wave function is symmetric with respect to the exchange of the two electrons, which have a non-zero probability of being at the same point in space. As a result, the electron repulsion energy becomes large when the electrons are near each other, increasing the energy of the singlet state. However, the orbital wave function of the triplet state is antisymmetric under the exchange of the two electrons. This leads to a zero probability of being at the same point in the space with smaller average electrostatic repulsion. The energy difference between singlet and triplet states arises because of the symmetrization postulate, even though spin does not appear explicitly in the Hamiltonian.

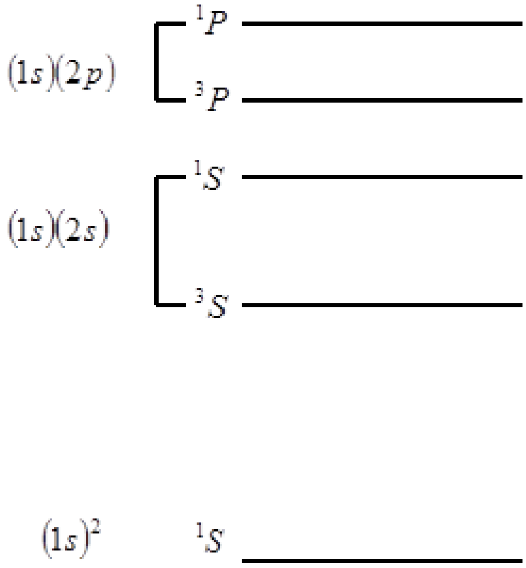

Figure 2.6: Schematic energy level diagram for low-lying configurations of the helium atom, showing exchange splitting of the $(1s)(2s)$ and $(1s)(2p)$ configurations. The general term symbol, ^{2S+1}L, is used in the above figure where S and L denote total spin and total orbital momentum quantum numbers respectively. The term, $2S+1$, describes spin multiplicity. For example, for the $(1s)(2s)$ configuration, one simply gets $S=0$, $L=0$ (singlet state) and $S=1$, $L=0$ (triplet state).

While substitutional sulfur or selenium impurities are double donors in silicon or germanium, beryllium and zinc are examples of double acceptors in silicon or germanium. Double acceptors are spectroscopically richer than neutral helium (He^0). Unlike He^0, there can be splitting of the ground state as well as bound excited states. In addition, splitting due to the exchange interaction is directly observable with IR spectroscopy because of the large spin-orbit coupling.

2.2.3 Wave function symmetry

Impurity wave functions can be classified according to their symmetry, where the symmetry is defined as a set of point-group of operations that do not change the defect [1]. In diamond and zincblende structures such as ZnTe, impurities have tetrahedral (T_d) symmetry. Impurities in wurtzite semiconductors such as ZnO possess trigonal (C_{3v}) symmetry.

A point group can also provide valuable information about the degeneracy of electronic states, important in the interpretation of absorption spectra. For example in a cubic crystal, the $2p$ orbital has threefold degenerate wavefuctions, proportional to x, y, or z. Perturbing the crystal along one direction, for instance in the z direction, lifts the degeneracy. In this case the p_z orbital will have different energy from that of p_x and p_y orbitals.

Table 2.1 illustrates a systematic way of classification of the symmetry of wave functions and their degeneracy of common point groups. The symmetry of the wave functions is given in Mulliken symbols and by the Koster notation. In the Koster notation Γ_1 is totally symmetric representation. The s orbitals of a hydrogen atom, for instance, have Γ_1 symmetry. Symmetries lower than Γ_1 are represented by other symbols. The last column of the table shows functions of a given symmetry. Functions in parenthesis are degenerate.

This principle can be illustrated by considering again the p orbitals in a zinc blend crystals. By adding an impurity to the crystal, one lowers to T_d symmetry. The three fold degenerate orbitals, p_x, p_y, and p_z (T_2 symmetry), are proportional to x, y, and z functions, respectively. However, in a wurtzite crystal the c axis is different from the a axes. As the symmetry of the point group lowers to C_{3v}, the orbitals are split into doubly degenerate E states (*x*,*y*) and one A_1 (*z*) states. Further reduction symmetry to C_s results in splitting into two nondegenerate *A*' states and one *A*'' state.

POINT GROUP	MULLIKEN	KOSTER	DEGENERACY	FUNCTIONS
T_d	A_1	Γ_1	1	$x^2 + y^2 + z^2$
	A_2	Γ_2	1	
	E	Γ_3	2	$(2z^2 - x^2 - y^2, x^2 - y^2)$
	T_1	Γ_4	3	
	T_2	Γ_5	3	$(x, y, z); (xy, xz, yz)$
C_{3v}	A_1	Γ_1	1	$z; x^2 + y^2; z^2$
	A_2	Γ_2	1	
	E	Γ_3	2	$(x, y); (x^2 - y^2, xy); (xz, yz)$
C_s	A'	Γ_1	1	$y; z; yz; x^2; y^2; z^2$
	A''	Γ_2	1	$x; xy; xz$
C_1	A	Γ_1	1	(All functions)

Table 2.1: Common point groups and wave function symmetries. The symmetries are indicated by Mulliken and Koster notations. (From Ref. [2].)

The ways these levels split can be summarized using *compatibility tables*. Table 2.2 shows the splitting of the T_2 into A_1 and E states, as one lowers the symmetry from T_2 to C_{3v}.

In table 2.3, we see that when the symmetry is lowered to C_s, the A_1 becomes A' and the E state splits into A' and A''.

T_d	C_{3v}
A_1	A_1
A_2	A_2
E	E
T_1	$A_2 \oplus E$
T_2	$A_1 \oplus E$

Table 2.2: Compatibility table for the T_d point group, showing the level splitting as the symmetry is lowered to C_{3v}. (From Ref. [2].)

C_{3v}	C_s	C_1
A_1	A'	A
A_2	A''	A
E	$A' \oplus A''$	$A \oplus A$

Table 2.3: Compatibility table for the C_{3v} point group, showing the level splitting as the symmetry is lowered to C_s or C_1. In both cases the doubly degenerate E level is lifted. (From Ref. [2].)

2.2.4 Acceptors wave functions

Acceptor wave functions are composed of the valence-band states at the Brillouin zone center, $k = 0$. Since the valence band is composed of p orbitals (l=1), it has a total angular momentum of j =3/2 since an electron spin is 1/2. Therefore one can consider a free hole with j =3/2. When the hole is bound by an acceptor, it has an envelope function, similar to the donor electrons. The total angular momentum of hole is given by

$$f = |j - l| ... j + l, \tag{2.24}$$

where l is the angular momentum of the envelope function. Using spectroscopic notation, the bound states of the acceptor can be written as:

$$nS_{3/2}, \text{ for } l = 0, \tag{2.25}$$

$$nP_{1/2}, \; nP_{3/2}, \; nP_{5/2}, \text{ for } l = 1, \tag{2.26}$$

where the subscripts denote the value of f. Generally the angular momentum with l< 2 are significant. Therefore the acceptors with the lowest energy states are $1S_{3/2}$, $2S_{3/2}$, $2P_{1/2}$, $2P_{3/2}$, and $2P_{5/2}$.

In the presence of T_d symmetry, while the energy levels of the $S_{3/2}$, $P_{1/2}$, and $P_{3/2}$ are only shifted, the degeneracy of the $P_{5/2}$ level splits into two levels [4].

References

[1]. F. A. Cotton, Chemical Application of Group Theory, (Wiley-Interscience, New York, 1971).

[2]. M. D. McCluskey, and E. E. Haller, Dopants and Defects in Semiconductors, (CRC Press, New York, 2012).

[3]. H. Eyring, J. Walter, and G. E. Kimball, Quantum Chemistry, (John Wiley, New York, 1944, p. 371).

[4]. A. Baldereschi, and L. O. Lipari, Phys. Rev. B **8,** 2697 (1973).

[5]. J. J. Sakurai, Modern Quantum Mechanics, (Addison-Wesley, New York, 1994).

Chapter 3 Experimental techniques

3.1 Fourier transform infrared (FTIR) spectroscopy

The main experimental technique employed in this work was Fourier transform infrared (FTIR) spectroscopy [1-3]. It is based on the interaction of electromagnetic radiation with a molecular system, mainly through the absorption of energy from the incident beam. The heart of a FTIR spectrometer is a Michelson interferometer, consisting of a beam splitter, a fixed mirror and a movable mirror (Fig. 3.1). A beam emitted by a source is separated into two parts and then recombines at a semitransparent beamsplitter. The recombined beam travels through the sample and finally hits the detector. The intensity of the output beam, the interferogram, is plotted as a function of the optical path difference (Fig. 3.2). A plot of intensity versus frequency can be obtained when the interferogram is Fourier transformed (Fig. 3.3).

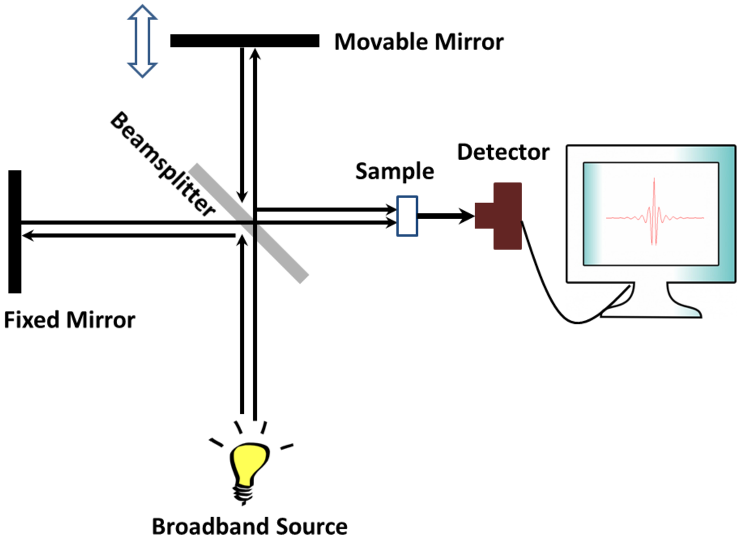

Figure 3.1: Schematic diagram of a FTIR spectrometer.

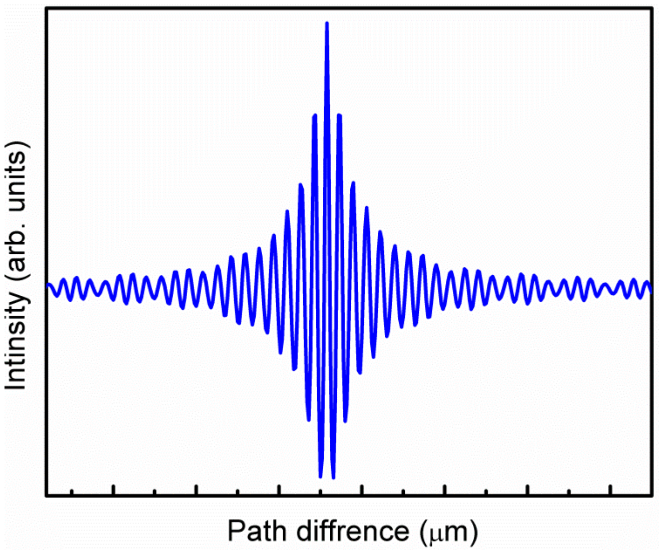

Figure 3.2: An example of an interferogram.

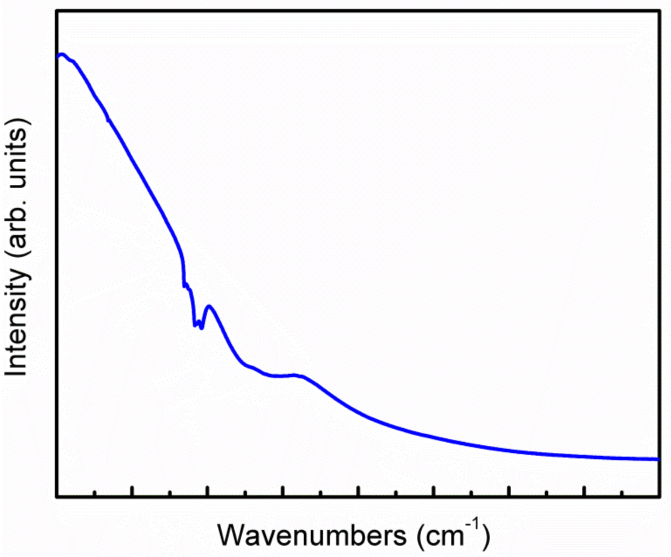

Figure 3.3: Fourier transformed spectrum.

3.1.1 Fourier transform technique

In this section I will follow the treatment given in Ref. [1] to show the relation between the interferogram and the IR spectrum. Let $y(z)$ and $E(k)$ be a Fourier pair which, mathematically, can be written as:

$$y(z) = \int_{-\infty}^{\infty} E(k)\exp(i2\pi kz)dk, \tag{3.1}$$

$$E(k) = \int_{-\infty}^{\infty} y(z)\exp(-i2\pi kz)dz. \tag{3.2}$$

Consider two electromagnetic waves, $y_1(z)$ and $y_2(z)$, which are separated by an optical path difference δ:

$$y_1(z) = \int_{-\infty}^{\infty} E(k)\exp(i2\pi kz)dk, \tag{3.3}$$

$$y_2(z) = \int_{-\infty}^{\infty} E(k)\exp\left[i2\pi k(z-\delta)\right]dk. \tag{3.4}$$

Eqs. (3.3) and (3.4) represent the two waves after recombination at the Beamsplitter. Using superposition principle, the recombined waves at the detector can be given as

$$y(z) = y_1(z) + y_2(z) = \int_{-\infty}^{\infty} \left[E(k)(1+\exp(-i2\pi k\delta))\exp(i2\pi kz)\right]dk. \tag{3.5}$$

By defining the resultant field $E(\delta, k)$ as

$$y(z) = \int_{-\infty}^{\infty} E(\delta,k)\exp(i2\pi kz)dk, \tag{3.6}$$

Comparison Eqs. (3.5) and (3.6) give us,

$$E(\delta,k) = E(k)\left[1+\exp(-i2\pi k\delta)\right]. \tag{3.7}$$

The intensity or irradiance $B(k,\delta)$ is given by

$$B(k,\delta) = \frac{1}{2}c\varepsilon_0 E^*(\delta,k)E(\delta,k), \tag{3.8}$$

where ε_0 is the electric permittivity of free space, c is the velocity of light in vacuum. Substituting Eq. (3.7) into Eq. (3.8) we get

$$B(\delta,k)=\frac{1}{2}c\varepsilon_0E^2(k)[2+\exp(-i2\pi k\delta)+\exp(i2\pi k\delta)]. \tag{3.9}$$

Using the definition of cosine, Eq. (3.9) can be simplified as

$$B(\delta,k)=c\varepsilon_0E^2(k)\left[1+\cos(2\pi\delta k)\right]. \tag{3.10}$$

For a broadband source the total intensity as a function of optical path difference, known as the interferogram, can be found by integrating over k :

$$I(\delta)=c\varepsilon_0\left[\int_0^\infty E^2(k)dk+\int_0^\infty E^2(k)\cos(2\pi\delta k)dk\right]. \tag{3.11}$$

For a zero path difference between the two beams ($\delta=0$), Eq. (3.11) becomes

$$\frac{1}{2}I(0)=c\varepsilon_0\int_0^\infty E^2(k)dk. \tag{3.12}$$

Substituting Eq. (3.12) into Eq. (3.11), we get

$$\left[I(\delta)-\frac{1}{2}I(0)\right]=\int_0^\infty c\varepsilon_0E^2(k)\cos(2\pi\delta k)dk. \tag{3.13}$$

Writing the Fourier transform of the above integral, we have

$$c\varepsilon_0E^2(k)=\int_0^\infty\left[I(\delta)-\frac{1}{2}I(0)\right]\cos(2\pi k\delta)d\delta. \tag{3.14}$$

Using the expression in Eq. (3.8), the final result becomes

$$B(k)=(\text{constant})\int_0^\infty\left\{\left[I(\delta)-\frac{1}{2}I(0)\right]\cos(2\pi k\delta)\right\}d\delta. \tag{3.15}$$

For the general case, one can write the above Eq. as

$$B(k)=\int_{-\infty}^\infty\left[I(\delta)-\frac{1}{2}I(0)\right]\exp(-i2\pi k\delta)d\delta. \tag{3.16}$$

To obtain the integral, a fast Fourier transform (FFT) method can be used [4].

3.1.2 Apodization and Resolution of a FTIR spectrometer

As shown in Eqs. (3.15) and (3.16), one would have to scan the moving mirror of the interferometer an infinitely long distance, which is impossible since the optical path difference of a FTIR spectrometer is finite. Apodization is a corrective procedure for modifying the basic Fourier transform integrals. The complete interferogram can be effectively multiplied by a boxcar truncation function, $f(x)$ [5]:

$$f(x) = 1 \quad \text{if} \quad |x| \le L, \tag{3.17}$$

$$f(x) = 0 \quad \text{if} \quad |x| > L.$$

The effect of multiplying the complete interferogram by the boxcar function is to get the convoluted Fourier transforms of both functions. The Fourier transform of a box car function is a function, $\mathrm{sinc}\,(x) = \sin(x)/x$, [Fig. 3.4(a)]. As shown in the figure, the maximum has a series of positive and negative side lobes, an artifact due to the abrupt truncation. The side lobes can be reduced by the process of apodization, correcting the interferogram by multiplying it with suitable apodization functions before applying FFT. The following are common apodization functions:

Triangular:

$$\begin{aligned} f(x) &= 1 - \frac{|x|}{L} && \text{if} \quad |x| \le L, \\ f(x) &= 0 && \text{if} \quad |x| > L. \end{aligned} \tag{3.18}$$

Norton-Beer [6]:

$$f(x)=\sum_{n=0}^{k}C_n\left[1-\left(\frac{x}{L}\right)^2\right]^n;\qquad \sum_{n=0}^{k}C_n=1. \tag{3.19}$$

Happ-Genzel [7]:

$$f(x)=a+b\cos\left(\frac{x\pi}{2L}\right). \tag{3.20}$$

Suppose one chooses a triangular apodization function. Its Fourier transform is $\mathrm{sinc}^2(x)=\sin^2(x)/x^2$. As can be seen in Fig. 3.4 (b), the side lobes are greatly reduced.

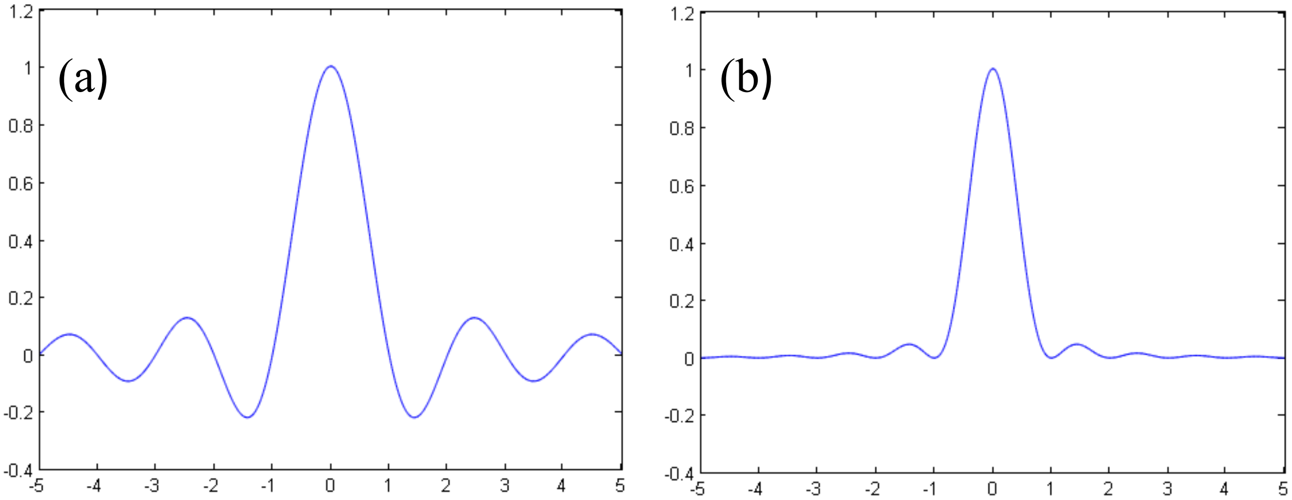

Figure 3.4: Plots of (a) $\sin(x)/x$ and (b) $\sin^2(x)/x^2$ functions.

The resolution, Δ in wavenumbers (cm^{-1}), of a FTIR spectrometer is inversely related to the maximum optical path difference $\delta_{\max}$ used to obtain the interferogram.

$$\Delta \sim \frac{1}{\delta_{\max}}. \tag{3.21}$$

3.1.3 Phase correction

Practically, the interferogram is not symmetrical about zero path difference (ZPD). This is because of the phase delays arising from experimental errors such as optical components, detector, or electronic filters. A complex spectrum, instead of the real spectrum, results from the Fourier transform of such an asymmetrical interferogram. Therefore it is necessary that the phase be corrected. Generally the complex spectrum, $S(k)$, from the asymmetric interferogram, and the true spectrum, $B(k)$, are related by the following equation:

$$S(k) = B(k)\exp[-i\Theta(k)], \tag{3.22}$$

where $\Theta(k)$ is the wavenumber-dependent 'phase' and it is given by:

$$\Theta(k) = \arctan\left\{\frac{\mathrm{Im}[S(k)]}{\mathrm{Re}[S(k)]}\right\}. \tag{3.23}$$

More details on phase correction method are given in Ref. [8].

3.1.4 Advantages of a FTIR

Comparing to the linear slits in grating spectrometers, FTIR spectrometers possess large area of circular aperture which allows one getting a higher throughput of radiation. This advantage is known as Jacquinot or throughput advantage.

Another advantage is due to multiplex or Fellget's advantage. In a FTIR spectrometer, all the frequencies from the source hit the detector simultaneously. However in a dispersive spectrometer, a particular spectral element is recorded in a particular time. The signal-to-noise ratio (SNR) of spectra measured on FTIR will be greater than the SNR spectrum recorded on a grating spectrometer measured at the same time. More details on advantages of a FTIR can be found Ref. [1, 2].

3.1.5 FTIR operation

IR spectra were obtained using Bomem DA8 FTIR spectrometer (Fig. 3.5). In this work, the spectrometer was equipped with a heated ceramic globar light source, KBr beam-splitter, and mercury cadmium telluride (MCT) or indium antimonide (InSb) detectors. The globar light source is a black body radiator which emits a broad spectrum of wavelengths as low as 200 cm^{-1}. The KBr beam splitter works best in the ranges of 450 – 4000 cm^{-1}. The detectors must be cooled down to liquid nitrogen temperatures to reduce thermally excited current. The MCT detector is sensitive to the IR light in the range of 450 – 5000 cm^{-1} but the InSb detector is much more sensitive in the range of 1600 – 7000 cm^{-1}.

In addition, the spectrometer has a vacuum system and an attached closed-cycle liquid-helium cryostat, capable of reaching 10 K, for low temperature measurements. Unwanted IR absorption of H_2O and CO_2 can be reduced by evacuating the spectrometer using the vacuum system.

A He-Ne laser, 632 nm, is used for an accurate position of the moving mirror. By measuring the interference pattern created when the He-Ne laser is passed through the Michelson interferometer, a high precision tracking of the path-length difference is achieved. A visible white source is used to determine zero-path-difference (ZPD). Well defined maximum intensity is produced at ZPD by a white light so that each mirror scan can be aligned and averaged before taking the Fourier transform.

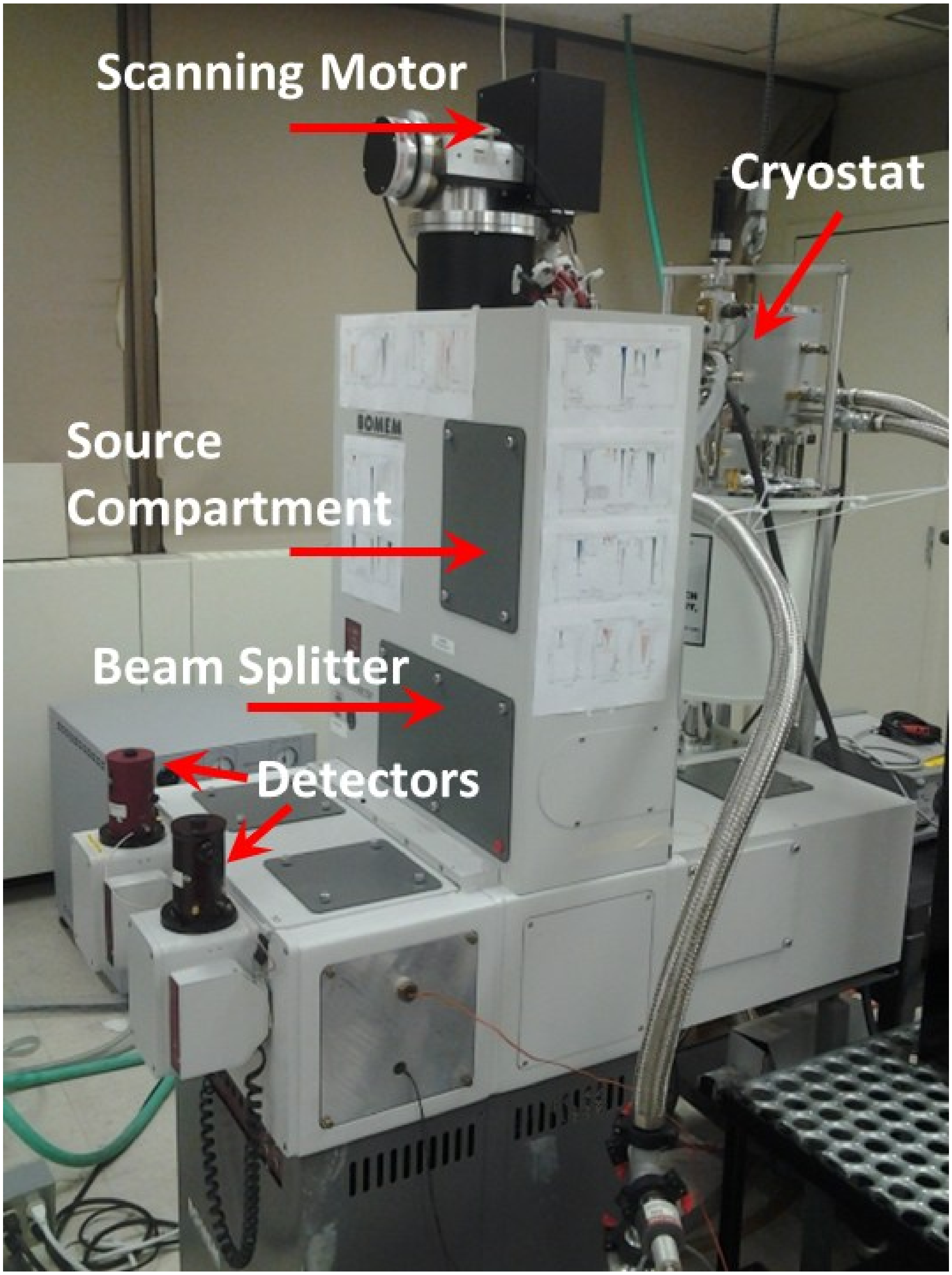

Figure 3.5: Bomem DA8 FTIR spectrometer showing the scanning motor, source compartment beam splitter, detectors (MCT and InSb) and the cryostat.

3.2 Photoluminescence (PL) spectroscopy

Photoluminescence is a process by which an optical excitation of a semiconductor and subsequent emission of the radiation by this system takes place. An emission process can simply be expressed as the inverse of an absorption process of which is given by

$$\text{Absorbance} = \log_{10}(I_0 / I) = -\log_{10}(T), \tag{3.24}$$

where I_0, I, and T are the incident intensity, transmitted intensity and transmission respectively. However, while an absorption process is described by a mean free path for photon decay, an emission process is described as a rate of photon generation per unit volume. In direct gap semiconductors such as ZnO, above gap light excites an electron from the valence band maximum to the conduction band minimum via a vertical transition in k, generating an electron-hole pair. After absorption of electromagnetic radiation, the generated electron-hole pairs recombine through either radiative or non-radiative processes which lead to an emission of photons with characteristic energies.

In this section, I will discuss the basics of the following typical PL processes, commonly observed in semiconductors materials. A reader is referred to Ref. [9-13] for more details on PL processes.

3.2.1 Band-to-impurity transition

Impurities in semiconductors can give rise to specific luminescence. The impurities could be either acceptors or donors on the crystal. Here I will consider an example of the presence of a neutral acceptor (A^0) in a semiconductor as shown in Fig. 3.6. An electron can be excited from the valence band to the conduction band by an energy which is higher than the band gap. This free electron at the bottom of the conduction band minimum can recombine with a hole trapped on the acceptor level. Such PL transition, known as band-to-impurity, emits a photon of energy

$$h\nu = E_g - E_a, \tag{3.25}$$

where h is the Planck's constant (6.626 X 10^{-34} Js), ν is the emitted photon frequency, E_g is the band gap energy and E_a is the acceptor binding energy.

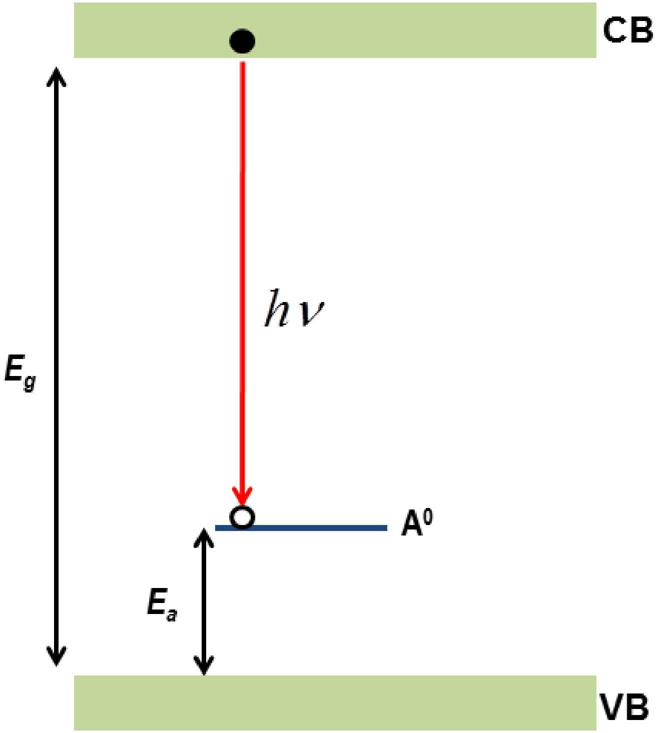

Figure 3.6: PL transition between a band and an acceptor impurity state.

Band-to-impurity transition is a simple way of determining an impurity binding energy in a semiconductor material. This type of transition, however, is limited to low impurity concentration (~10^{17} cm^{-3}). If the acceptor concentration becomes large (~10^{20} cm^{-3}) the impurity band could eventually merge with the valence band [10]. In such situation, the holes are no longer localized on the acceptors and become free carriers.

3.2.2 Donor-Acceptor pair transitions

Quite often there is a situation where both donors and acceptors are simultaneously present in semiconductors. In such case, the electrons from neutral donors (D^0) can recombine radiatively with the holes in neutral acceptors (A^0), resulting in ionized donors (D^+) and acceptors (A^-). Above gap light creates electrons and holes in the conduction and valence bands, respectively. The carriers can become trapped and neutralize the D^+ and A^-, producing D^0 and A^0, and the process resumes. Fig. 3.7 shows a donor-acceptor pair transition process (DAP transition). Such PL process can be described by the following reaction.

$$D^0 + A^0 \rightarrow D^+ + A^- + h\nu. \tag{3.26}$$

Taking into account the Coulomb interaction between D^+ and A^-, the energy of the emitted photon will be

$$h\nu = E_g - E_d - E_a + \frac{e^2}{4\pi\varepsilon\varepsilon_0 R}, \tag{3.27}$$

where E_g is the band gap energy; E_d and E_a are the donor and acceptor binging energies, respectively. ε is the dielectric constant and R is the distance between the donor and the acceptor. Eq. (3.26) holds true provided that R is much larger than the lattice constant. We notice that the emitted photon energy is increased by the last term of Eq. (3.27).

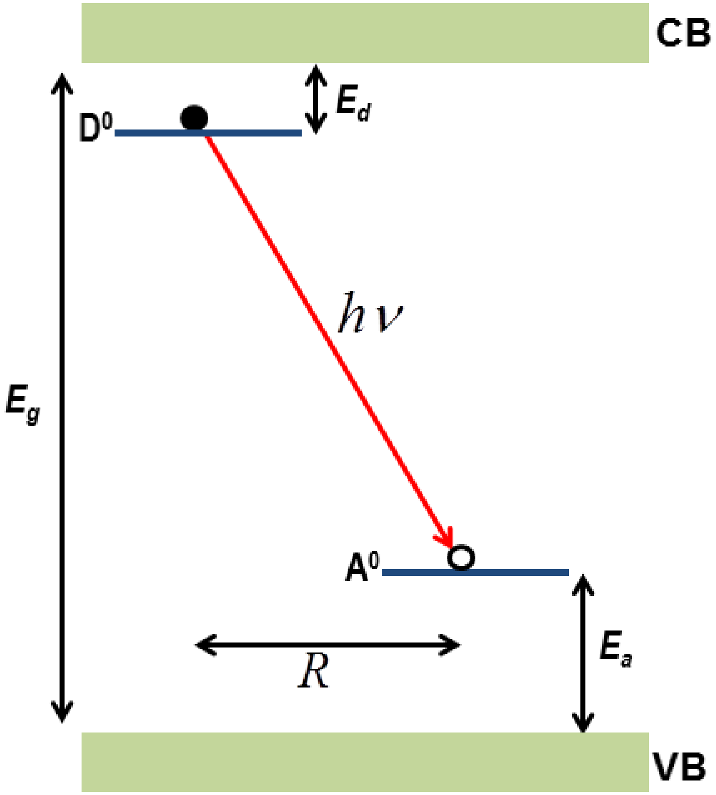

Figure 3.7: An example of PL process where donor-acceptor pair transition takes place. *R* is the distance between the donor and acceptor atoms.

In this work, PL experiments utilized a JY-Horiba FluroLog-3 [14] spectrometer consisting of an excitation source of 450 W xenon CW lamp, double-grating excitation and emission monochromators (1200 grooves mm^{-1} grating) and a R928P photomultiplier tube (PMT) as shown in Fig. 3.8. A beam of light from the source is filtered by an excitation monochromator that allows a single wavelength of light to reach the sample. The sample responds to the incoming radiation in the sample compartment and the resulting radiation is filtered by an emission monochromator that feeds the signal to the PMT detector. By stepping either or both monochromators through a wavelength region, and recording the variation in intensity as a function of wavelength, a spectrum is produced.

The double-grating excitation and emission monochromators make the Flurolog-3 model capable of having improved performance in resolution, sensitivity, and stray-light rejection. To improve the quality of the acquired data, the system allows the user with multiple options. A high signal-to-noise ratio, for instance, can be obtained by using an appropriate integration time, scanning a region several times and averaging the results, changing the bandpass by adjusting the slit-widths, and smoothing the data mathematically.

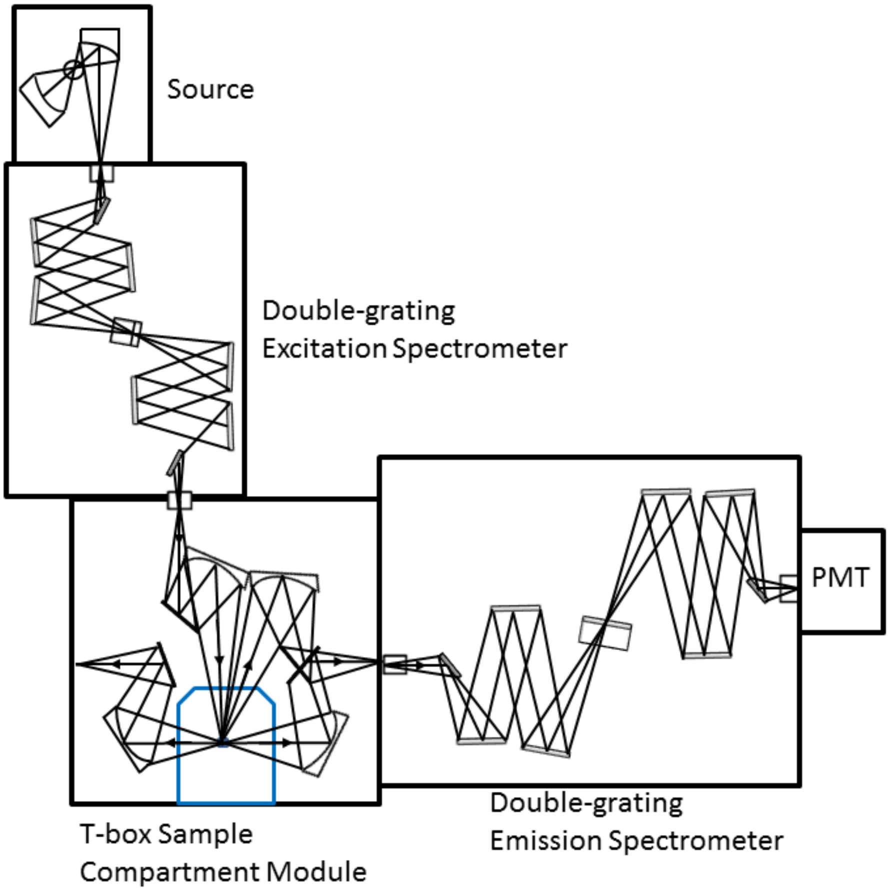

Figure 3.8: Schematic diagram of Fluorolog-3, showing the source, double-grating excitation and emission spectrometers, sample compartment module and PMT.

3.3 Electron paramagnetic resonance (EPR) spectroscopy

Magnetic resonance spectroscopy is a powerful technique used to characterize defects in semiconductors. The theory behind the subject is briefly given by Abragam and Bleaney [13] or McCluskey and Haller [11]. The electron paramagnetic resonance (EPR) technique uses microwave energy to detect unpaired electron spins. Defects in crystals that contain an unpaired spin are EPR active.

The principle behind EPR can be understood when an electron is immersed in an external magnetic field that points in the z direction. The z component of the electron spin magnetic moment, μ_z, is given by

$$\mu_z = -g\mu_B m_s, \tag{3.28}$$

where $g = 2.00232$ for a free electron, μ_B is the Bohr magneton ($9.274*10^{-24}$ Joule/Tesla), and $m_s = \pm$ ½. The energy E of a magnetic moment in a magnetic field **B** can be written as

$$E = -\boldsymbol{\mu} \cdot \mathbf{B} = g\mu_B B m_s. \tag{3.29}$$

Therefore, the two spin-state (spin up and spin down) energy levels are given by the electronic *Zeeman* energies, $E = \pm\frac{1}{2}g\mu_B B$ as shown in Fig. 3.9. The separation in energy is proportional to B and is given by

$$\Delta E = g\mu_B B. \tag{3.30}$$

By matching ΔE with the appropriate photon energy $h\nu$, known as resonance condition, an EPR transition can be induced from a spin-down to a spin-up state.

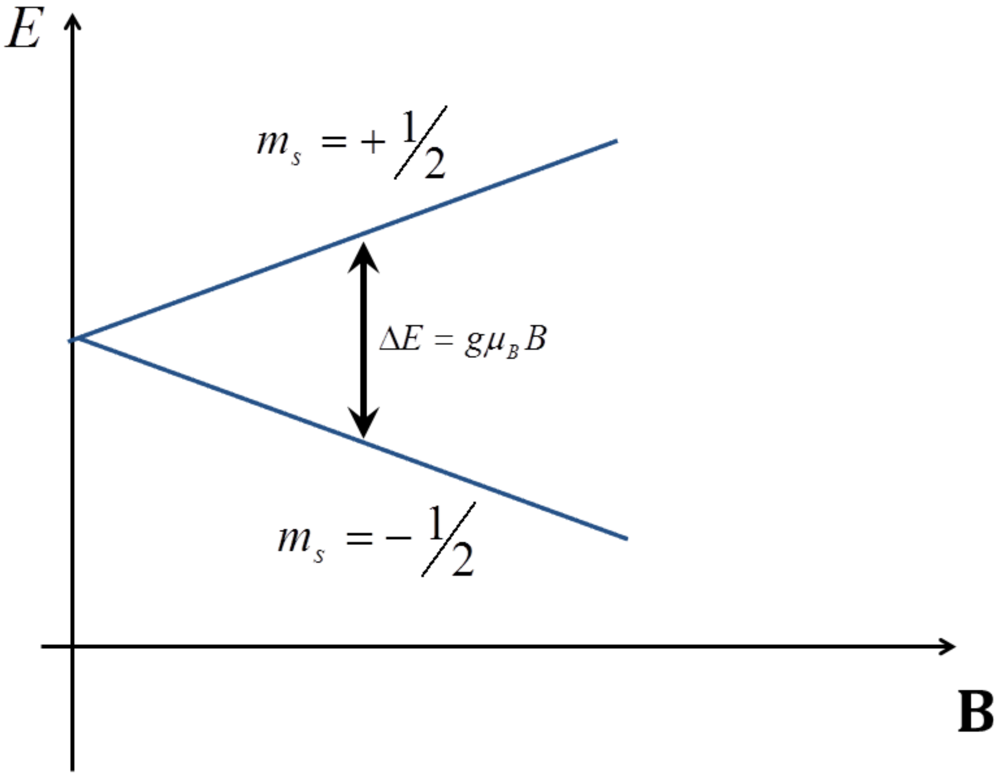

Figure 3.9: Schematic of Zeeman splitting for an electron of spin S = ½. The resonance position is indicated by the vertical arrow.

Experimentally, it is more practical to keep the microwave frequency fixed while sweeping the magnetic field. For a magnetic field of 340 mT and $g = 2$, the frequency will be ~ 9.5 GHz, which is in the microwave region (X-band) of the electromagnetic spectrum.

Eq. (3.30) is not a complete story for an EPR experiment of materials. In reality, the orbital angular momentum induced on the neighboring atoms by the spin produces deviations of the g factor from the free-electron value. For a complete EPR treatment, interactions with the crystal field, other electrons, and nuclear magnetic and electric quadrupole moments should be considered [15].

The EPR experiments were performed using a user facility at the Environmental Molecular Science Laboratory (EMSL), located at Pacific Northwest National Laboratory (PNNL). In this work a Bruker 380E EPR spectrometer, with an operating frequency of ~ 9.38 GHz, was used for an X-band experiment. An EPR experiment was also conducted using a high field, W-band, EPR spectrometer which operates at 95 GHz. In both experiments, the sample temperature was held at 77 K.

3.4 Electrical measurements

3.4.1 Conductivity and Resistivity

The electrical conductivity σ of a material is given by:

$$\sigma = ne\mu, \tag{3.31}$$

where n is the free-carrier concentration, e is the charge of an electron, and μ is the mobility. The resistivity ρ is defined as the inverse of the conductivity:

$$\rho = \frac{1}{ne\mu}. \tag{3.32}$$

3.4.2 Hall Effect

The Hall effect is used to determine the free-carrier type and concentration [11]. Fig. 3.10 shows a standard Hall effect configuration where a magnetic field is applied in z direction and a current is flowing in the x direction. A moving charged particle in the presence of an electric and magnetic field experience a Lorenz force:

$$\mathbf{F} = e(\boldsymbol{E} + \mathbf{v}\,\mathrm{X}\,\mathbf{B}). \tag{3.33}$$

The force due to the magnetic field pushes the carriers in the $-y$ direction, resulting to an electric field, $\mathbf{E_H}$, pointing in the y direction. At equilibrium the Lorentz force becomes:

$$e(\mathbf{v} \,\mathrm{X}\, \mathbf{B}) = -e\mathbf{E_H} \,. \tag{3.34}$$

From Fig. 3. 10, the Hall effect is given by

$$E_H = Bv_x, \tag{3.35}$$

where v_x is the drift velocity along the x direction.

The Hall coefficient is defined as

$$R_H = \frac{E_H}{j_x B}, \tag{3.36}$$

where j_x is the x component of the current density which is given by $j_x = nv_x e$. Therefore Eq. (3.36) becomes

$$R_H = \frac{1}{ne}. \tag{3.37}$$

this gives the expression for the carrier concentration n. The mobility can be given by

$$\mu = \frac{j_x}{neE_x}. \tag{3.38}$$

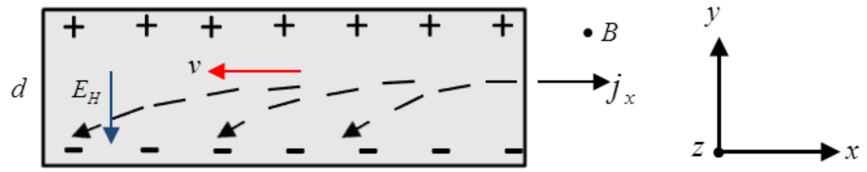

Figure 3.10: Standard Hall-effect configuration.

Hall-effect measurements are can easily be made using a 4-probe method called Van der Pauw geometry [16] which uses an arbitrary shaped samples. As shown in Fig. 3.11 (a), an electric current i enters the sample at 1 and leaves at 2 and the potential difference between 4 and 3 is ΔV. The resistance R_1, is defined as:

$$R_1 = \frac{V_4 - V_3}{i}. \tag{3.39}$$

In (b), the leads are rearranged so the current enters the sample at 2 and leaves at 3 and the potential between 1 and 4 is measured. The resistance R_2, is given by

$$R_2 = \frac{V_1 - V_4}{i}. \tag{3.40}$$

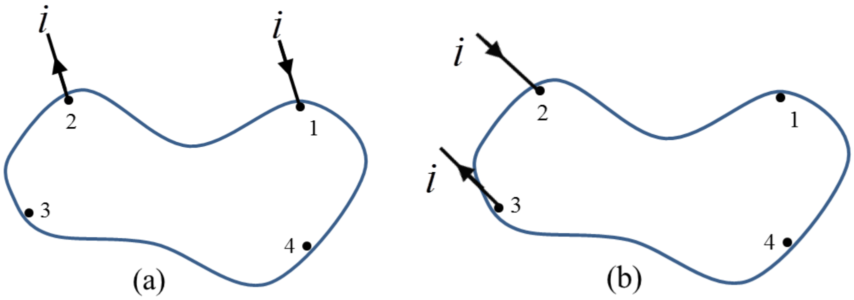

Figure 3.11: Van der Pauw geometry for resistivity measurements showing connections for (a) R_1 and (b) R_2.

By using conformal mapping, Van der Pauw showed that for flat conductive samples of arbitrary shape the resistivity ρ of the material is given by

$$\exp(-\pi d R_1/\rho) + \exp(-\pi d R_2/\rho) = 1, \tag{3.41}$$

where d is thickness of the sample. Eq. (3.41) can be simplified as

$$\rho = \frac{\pi d}{\ln(2)} \frac{R_1 + R_2}{2} f(R_1/R_2). \tag{3.42}$$

In most cases, the samples are nearly circular or square shaped, and $f \approx 1$.

In this work, the resistivity for samples of ZnO:Al films were obtained using MMR Technologies, Inc. variable Hall measurement system, capable of operating a temperature range from 80 K to 700 K.

3.5 Film deposition by sputtering

Magnetron sputtering is a plasma vacuum coating technique used to deposit a thin film of a material onto a substrate [17]. In sputtering, a material is ejected from a target by bombarding with argon atoms. The target atoms deposit on a sample in the vacuum chamber, resulting in a thin- film coating. The plasma is concentrated by a magnetron around the target.

In this work, ZnO:Al film deposition was performed using a BOC Edwards Auto 306 Sputter Machine at Washington State University, Center for Materials Research (CMR), shown in Fig. 3.12. The system consists of two main parts, the electronics stack and the machine housing. Most of the control devices for the system are contained in the electronics stack. This includes RF power supply, argon flow control, and magnetron selector switch. The vacuum chamber, where the sputtering process occurs, and process control panel are the main components of the electronics stack. The stack components mainly provide an input to the vacuum chamber for the sputtering process.

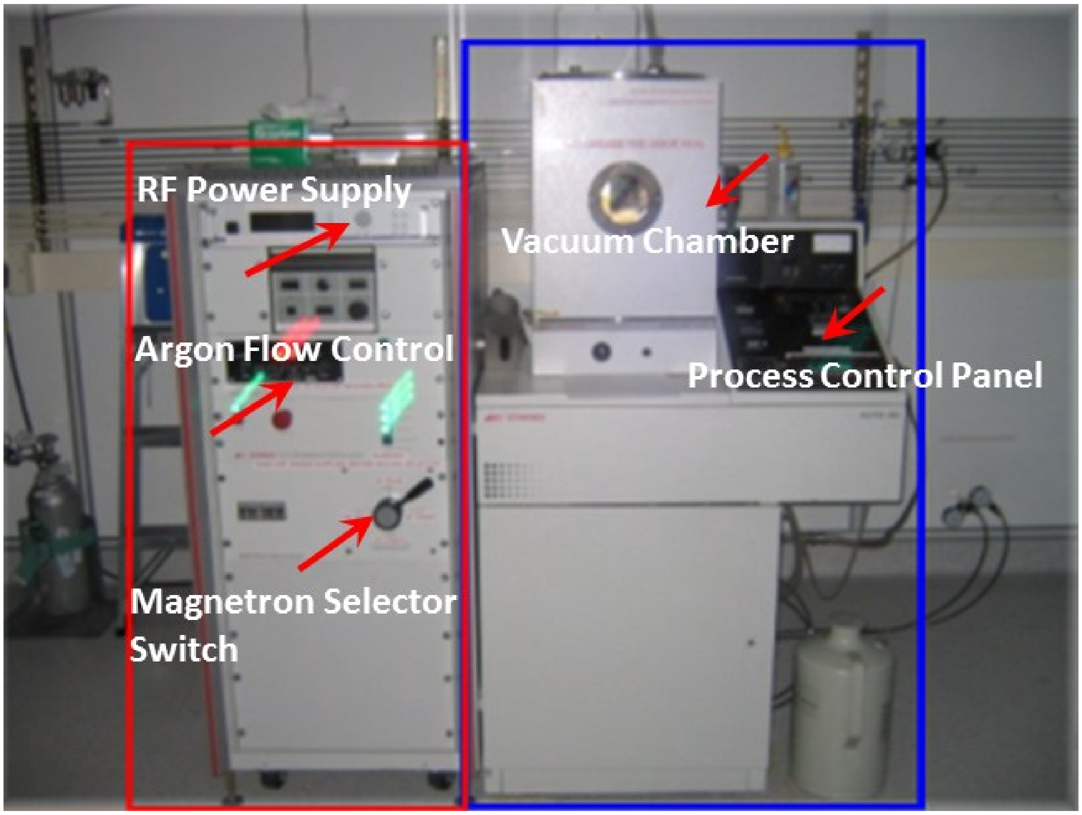

Figure 3.12: BOC Edwards Auto 306 Sputter Machine, showing its components.

3.6 Sample preparation for ZnO pellets

For IR spectra, solid pellets were made from a powder of ZnO nanoparticles using a commercial hand press and die sets. Part of the hand press, a movable cylinder press, is used for applying pressure onto the powder, which is loaded into a die set of 7 mm diameter. An adjustable dial is used to set the position of the press. By controlling the exerted force onto the powder, a pellet of thickness ~ 0.25 mm was prepared. In order to remove hydroxyl related surface species, samples were baked out at 323 K inside the cryostat under vacuum before cooling down to low temperature.

References

[1]. R. J. Bell, *Introductory Fourier Transform Spectroscopy* (Academic Press, New York, 1972).

[2]. P. R. Griffiths and J. A. de Haseth, *Fourier Transform Infrared Spectrometry* (Wiley, New York, 1986).

[3]. S. Wartewig, *IR and Raman Spectroscopy: Fundamental Processing* (WILEY-VCH Verlag GmbH & Co. KGaA, Weinheim, 2003).

[4]. J. W. Cooley and J. W. Tukey, Math. Computat. **19,** 297 (1965).

[5]. J. F. Rabolt and R. Bellar, Appl. Spectroscopy **35,** 132 (1981).

[6]. R. H. Norton and R. Beer, J. Opt. Soc. Am. **66,** 259 (1976).

[7]. H. Happ and L. Genzel, Infrared Phys. **1,** 39 (1961).

[8]. M. L. Forman, W. H. Steel and G. A. Vanasse, J. Opt. Soc. Am. **56,** 59 (1966).

[9]. A. Othanos and C. Christofides, Effect of Disorder and Defects in Ion-Implanted Semiconductors: Optical and Photothermal Characterization. In *Semiconductors and Semimetals* Vol. 46, ed. R. K. Willardson and A. C. Beer, pp. 74-76 (Academic Press, San Diego, 1997).

[10]. J. I. Pankove, *Optical Processes in Semiconductors*, (Dover, New York, 1971).

[11]. M. D. McCluskey and E. E. Haller, *Dopants and Defects in Semiconductors*, (CRC Press, New York, 2012).

[12]. I. Pelant and J. Valenta, *Luminescence Spectroscopy of Semiconductors*, (Oxford University Press, New York, 2012).

[13]. P. Y. Yu and M. Cardona, Fundamentals of Semiconductors, (Springer-Verlag, Berlin, 1996)

[14]. Fluorolog-3 Spectrofluorometer Operation Manual.

[15]. A. Abragam and B. Bleaney, Electron Paramagnetic Resonance of Transition Ions (Oxford University Press, 1970).

[16]. L. J. Van der Pauw, Philips Res. Rep. **13,** 1 (1958).

[17]. D. M. Mattox, Handbook of Physical Vapor Deposition (PVD) Processing (Noyes Publication, Park Ridge, NJ, 1998)

Chapter 4 Acceptors in as-grown zinc oxide nanocrystals

4.1 Introduction

As I discussed in the introduction part of section 1.4.1, the lack of reliable *p*-type doping has prevented ZnO from widespread use in optoelectronic applications. All proposed acceptor dopants, including the most investigated dopant N, form deep levels [1-6]. In this chapter, we provide evidence that ZnO nanocrystals contain hydrogenic acceptors *as grown*. Analogous to the hydrogen atom, hydrogenic acceptors give rise to electronic transitions that can be observed in the IR [7].

4.2 Synthesis of ZnO nanoparticles

ZnO nanoparticles were synthesized by solid-state pyrolytic reaction process [8-10]. In this method, zinc acetate dihydrate [$Zn(CH_3COO)_2 \cdot 2H_2O$] and sodium hydrogen carbonate ($NaHCO_3$) are reacted at 200 ^oC for 3 hr in an open-air furnace. Details are given in Ref. [9]. Transmission electron microscopy showed that the particles have an average diameter of ~20 nm (Fig. 4.1). The nano-powder was pressed into pellets of thickness ~ 0.25 mm with a diameter of 7 mm.

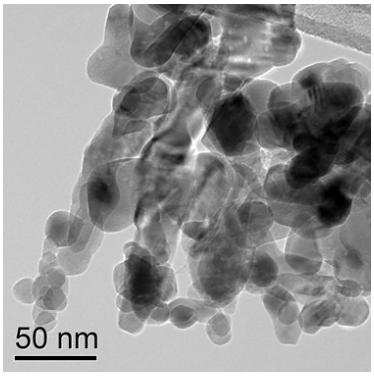

Figure 4.1: TEM image of ZnO nanoparticles.

4.3 Hydrogenic acceptors

Low temperature (10 K) IR absorption spectra were obtained with a Bomem DA8 Fourier transform infrared (FTIR) spectrometer. A KBr beamsplitter and InSb detector were employed for the spectral range of 1800 cm^{-1} – 7000 cm^{-1}, with an instrumental resolution of 2 cm^{-1}. In order to remove hydroxyl related surface species, the sample was baked out at 323 K inside the cryostat under vacuum before cooling down to low temperature.

Figure 4.2 shows an IR absorption spectrum for the as-grown ZnO nanoparticles. The IR absorption spectrum was calculated using Absorbance = $\log_{10}(I_R/I)$, where I_R and I are the transmission spectra for no sample (blank) and an as-grown sample, respectively. A quadratic baseline was then subtracted from the absorbance spectrum. A series of peaks is observed in the energy range of 425 – 457 meV. This result is suggestive of a hydrogenic acceptor spectrum with a hole binding energy of 0.4 – 0.5 eV. Peaks did not shift in frequency for samples grown with deuterated precursors, which argues against the involvement of hydrogen. Na acceptor atoms were ruled out by growing nanocrystals using Li precursors, which showed the same set of lines.

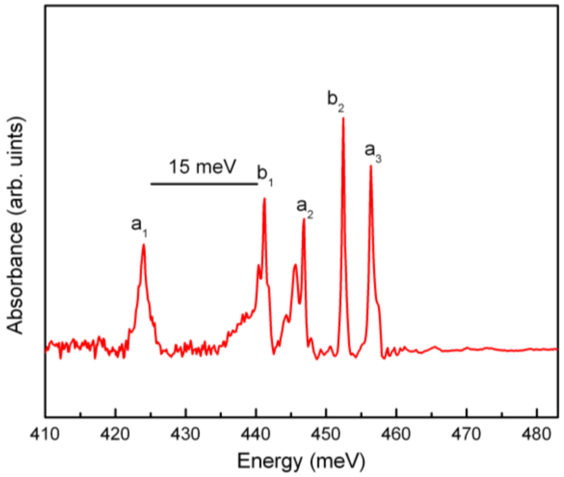

Figure 4.2: Low temperature (10 K) IR spectrum of ZnO nanocrystals showing electronic transitions.

4.4 Electronic transitions

The series of IR absorption peaks is similar to those observed in other II-VI compound semiconductors, such as shallow [11] and deep [12, 13] acceptor levels in cubic ZnTe. The transition energies are explained in the framework of the theory of Baldereshi and Lipari [14]. In this theory, within the spherical approximation, the acceptor Hamiltonian reduces to that of a hydrogen atom modified by a spherical "spin-orbit" term, which can be thought as a spin-3/2 particle in a Coulomb potential. When the cubic term in the Hamiltonian is included, the symmetry lowers to that of the point group T_d. The wave functions of the holes are classified according to the irreducible representations of this point group.

For the wurtzite crystal structure of ZnO, the point-group symmetry is C_{3v}. The crystal field and spin-orbit coupling split the valence band into three bands labeled *A*, *B*, and *C* (Fig. 4.3). At low temperatures, the energy difference between *A* and *B* excitons has been reported to be 15 meV [15]. As shown in Fig. 4.2, the sets of lines labeled *a* and *b* are offset by ~15 meV. We assign these transitions to excited states with holes originating from the *A* and *B* valence bands, respectively.

The envelope functions of the ground state have nonzero probability densities at the acceptor core, leading to a central-cell correction. However, the excited *P* states are less sensitive to central cell corrections and are best described by hydrogenic wavefunctions. In a single hole picture, the *A* valence band in C_{3v} symmetry gives rise to a hole wavefunction with Γ_4 symmetry (double group notation). The acceptor *P* wavefunctions belong to the representations $\Gamma_1 \times \Gamma_4 = \Gamma_4$ and $\Gamma_3 \times \Gamma_4 = \Gamma_4 + \Gamma_5 + \Gamma_6$. The *B* valence band has Kramers doublet (Γ_5, Γ_6) symmetries, where Γ_5 and Γ_6 are degenerate in the absence of an applied magnetic field. Figure 4.3 shows the allowed acceptor levels and hole transitions (Appendix A), along with their assignments. The observation of five main IR peaks is in agreement with our group-theoretical analysis. The side bands of b_1 and a_2 could be due to a slight reduction of symmetry, from C_{3v} to C_s.

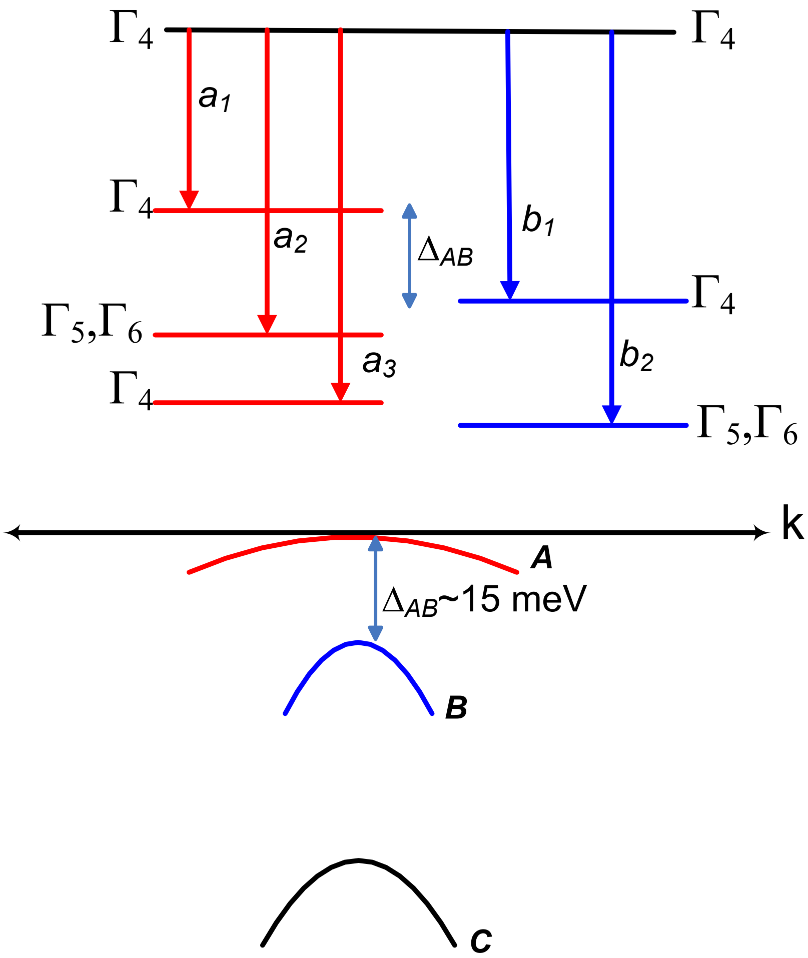

Figure 4.3: Schematic energy-level diagram of ZnO showing acceptor levels and splitting of the valence band. Hole transitions, which give rise to IR absorption peaks, are indicated by the arrows.

4.5 Electron paramagnetic resonance (EPR) results

Electron paramagnetic resonance (EPR) measurements were carried out with a Bruker 380E X-band spectrometer operating at 9.38 GHz and a sample temperature of 77 K. The measurements showed resonances at $g = 1.96$ and $g = 2.003$ in as-gown ZnO nanocrystals in the dark, prior to illumination by a xenon lamp (Fig. 4.4). The $g = 1.96$ resonance is associated with shallow donors [16]. We attribute the resonance at $g = 2.003$ to hydrogenic acceptors. A new signal at $g = 2.013$ appears after illumination. This center is consistent with nonaxial V_{Zn}-H complexes, which were observed in electron-irradiated, bulk ZnO after illumination with 325 nm laser light [17]. The V_{Zn}-H complexes are partially passivated Zn vacancies, with a hole residing on one of the nonaxial O atoms. Exposure to light transforms $(V_{Zn}\text{-H})^-$, which is EPR-inactive, to $(V_{Zn}\text{-H})^0$. The light also creates new centers near $g = 2.003$, which are attributed to axial V_{Zn}-H.

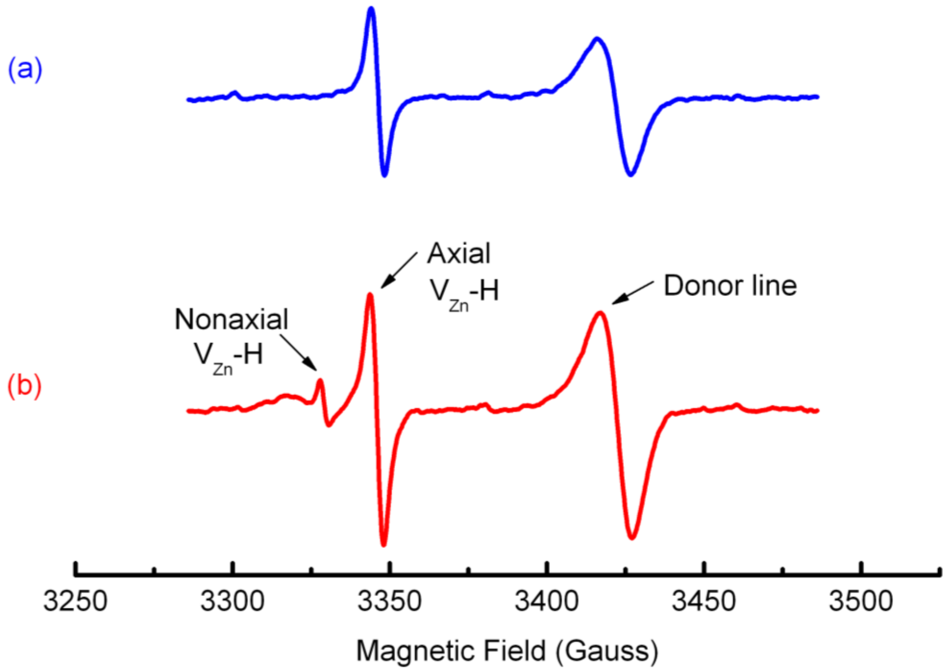

Figure 4.4: EPR spectra of ZnO nanocrystals taken at 77K. (a) Before illumination. (b) After illumination for 12 min by a xenon lamp.

In bulk ZnO, the EPR signatures for $g = 2.003$ acceptors only appear after illumination [17]. This is because, in the dark, the acceptors are fully compensated by donors and are EPR-inactive. ZnO nanocrystals, in contrast, appear to contain *uncompensated* acceptors. There are two possible reasons for this. First, the nonequilibrium growth conditions may result in a high concentration of vacancy defects [18]. Second, some of the nanocrystals may contain one acceptor and no donors, simply due to the small number of atoms in the nanocrystals [10].

4.6 Conclusions

We have studied defect properties of ZnO nanocrystals at low temperature using IR and EPR spectroscopy. The observed IR transition lines are consistent with a hydrogenic acceptor hole binding energy of 0.4 - 0.5 eV. EPR measurements show that some of the nanocrystals contain vacancy-hydrogen complexes (V_{Zn}-H). Given the existence of these complexes, it is reasonable to speculate that the observed hydrogenic acceptor may be vacancy-related. While V_{Zn}^- and V_{Zn}-H acceptors are deep [19], the acceptor level for the neutral vacancy (V_{Zn}^0) is predicted to lie 0.2 eV above the valence- band maximum [20]. Our EPR measurements, however, did not detect the V_{Zn}^0 signature [21]. A second possibility is a V_{Zn} - donor complex, which could contribute to the EPR resonance at $g = 2.003$ [16]. Considering the lack of suitable acceptor dopants in ZnO, these defect complexes merit additional investigation.

References

[1]. C. H. Park, S. B. Zhang, and S.-H. Wei, Phys. Rev. B **66,** 073202 (2002).

[2]. O. F. Schirmer, J. Phys. Chem. Solids **29**, 1407 (1968).

[3]. Y. Kanai, Jpn. J. Appl. Phys., Part 1 **30,** 703 (1991).

[4]. M. D. McCluskey and S. J. Jokela, J. Appl. Phys. **106,** 071101 (2009).

[5]. J. L. Lyons, A. Janotti, and C. G. Van de Walle, Appl. Phys. Lett. **95**, 252105 (2009).

[6]. M. C. Tarun, M. Z. Iqbal, and M. D. McCluskey, AIP Advances **1,** 022105 (2011).

[7]. A. Onton, P. Fisher, and A. K. Ramdas, Phys. Rev. **163,** 686 (1967).

[8]. Z. Wang, H. Zhang, L. Zhang, J. Yuan, S. Yan, and C. Wang, Nanotechnology **14,** 11 (2003).

[9]. W. M. Hlaing Oo, M. D. McCluskey, A. D. Lalonde, and M. G. Norton, Appl. Phys. Lett. **86,** 073111 (2005).

[10]. W. M. Hlaing Oo, M. D. McCluskey, J. Huso, and L. Bergman, J. Appl. Phys. **102,** 043529 (2007).

[11]. S. Nakashima, T. Hattori, P. E. Simmonds, and E. Amzallag, Phys. Rev. B **19,** 3045-3052 (1979).

[12]. K. Saminadayar, N. Magnea, J. L. Pautrat, and B. Pajot, Phys. Stat. Sol (b) **106,** 215 (1981).

[13]. G. Chen, I. Miotkowski, and A. K. Ramdas, **arXiv:0904.4284v1** [cond-mat.materl-sci] 2009.

[14]. A. Baldereschi and N.O. Lipari, Phys. Rev. B **9,** 1525-1539 (1974).

[15]. C. Boemare, T. Monteiro, M. J. Soares, J. G. Guilherme, and E. Alves, Physica B **308-310,** 985 (2001).

[16]. N. Y. Garces, N. C. Giles, L. E. Halliburton, G. Cantwell, D. B. Eason, D. C. Reynolds, and D. C. Look, Appl. Phys. Lett. **80,** 1334 (2002).

[17]. L. A. Kappers, O. R. Gilliam, S. M. Evans, L. E. Halliburton, and N. C. Giles, Nucl. Instrum. Methods Phys. Res. B **266,** 2953 (2008).

[18]. V. Ischenko, S. Polarz, D. Grote, V. Stavarache, K. Fink, and M. Driess, Adv. Funct. Mater. **15,** 1945 (2005).

[19]. X. J. Wang, L. S. Vlasenko, S. J Pearton, W. M. Chen, and I. A. Buyanova, J. Phys. D **42,** 175411 (2009).

[20]. A. Janotti and C. G. Van de Walle, Phys. Rev. B **76,** 165202 (2007).

[21]. S. M. Evans, N. C. Giles, L. E. Halliburton, and L. A. Kappers, J. Appl. Phys. **103,** 043710 (2008).

Chapter 5 Acceptor and surface states in zinc oxide nanocrystals: A unified model

In chapter 4 we provided evidence that ZnO nanocrystals contain acceptors as grown. The position of acceptor levels could be especially important at the interface between metals and ZnO nanocrystals, which have been reported to exhibit large second harmonic generation [1]. In this chapter, we present experimental evidence, using infrared (IR) and photoluminescence (PL) measurements, which allow us to determine the acceptor level, along with the intragap surface states responsible for red luminescence centered around 1.84 eV.

5.1 Experimental

The synthesis of ZnO nanoparticles used in this study is similar to that described in chapter 4. IR spectra were obtained with a Bomem DA8 Fourier transform infrared spectrometer with a KBr beamsplitter and liquid-nitrogen cooled InSb detector. Low-temperature measurements were performed in an attached closed-cycle liquid-helium cryostat capable of reaching 10 K. PL experiments utilized a JY-Horiba FluroLog-3 spectrometer consisting of double-grating excitation and emission monochromators (1200 grooves/mm grating) and an R928P photomultiplier tube (PMT). The PL spectra were obtained under the excitation source of 450-W xenon CW lamp with an instrumental correction for the wavelength dependent PMT response, grating efficiencies, and the variation in the output intensity from the lamp. The IR and PL spectral resolutions were 2 cm^{-1} and 1-3 nm, respectively.

5.2 Acceptor ionization

In Chapter 4 we showed a low temperature (10 K) series of IR absorption peaks, in the energy range of 0.425 - 0.457 eV, for the as-grown ZnO nanoparticles. The result was characteristic of a hydrogenic acceptor spectrum with a hole binding energy of 0.4 - 0.5 eV. These peaks were assigned to transitions to excited states with holes originating from the *A* and *B* valence bands. Although the identity of the acceptor was not determined, electron paramagnetic resonance measurements suggested that it may be a vacancy complex.

Figure 5.1 shows the temperature dependence of the integrated area, for one of the IR peaks, indicating consistent results upon cooling and warming the sample. The inset shows the IR peak, corresponding to a hydrogenic excited state, decreasing with temperature. The disappearance of the peak at high temperatures is evidence of thermal ionization of the acceptors. The solid line is a fit according a Boltzmann distribution function,

$$\alpha(T) = \alpha_0 / [1 + g \exp(-\Delta E/k_B T)] \, , \tag{5.1}$$

where α_0 is a constant, g is a degeneracy factor, ΔE is an activation energy, k_B is the Boltzmann constant and T is temperature (K). The fit yields $\Delta E = 0.08 \pm 0.006$ eV and $g = 176 \pm 67$.

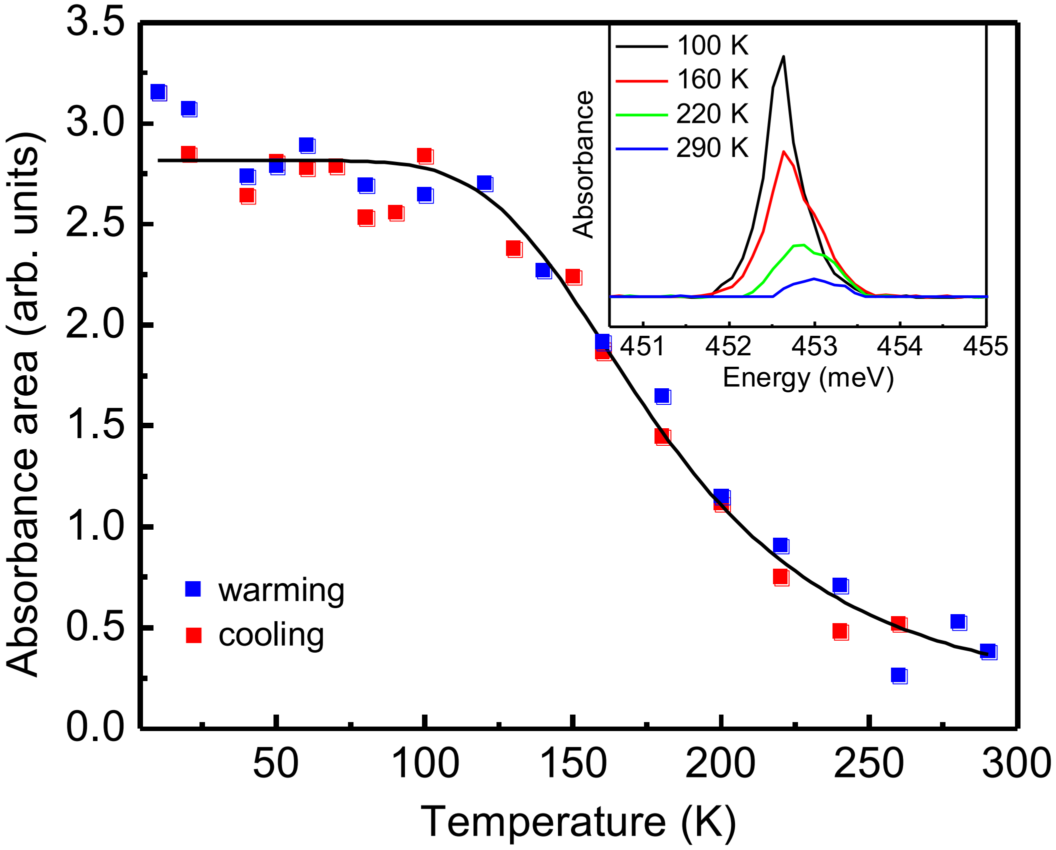

Figure 5.1: Temperature-dependent IR absorbance area of the acceptor excited-state peak upon cooling and warming of the sample. The solid line represents the fitting to the Boltzmann distribution function [Eq. (5.1)]. Inset: IR absorption spectra of an acceptor peak, showing a decrease with temperature.

5.3 Acceptor and surface states: A unified model

The activation energy ΔE is much lower than the hole binding energy of 0.46 eV. We propose that the holes are thermally excited from the acceptor ground state to a band of surface states that lies 0.38 eV above the valence-band maximum (Fig. 5.2). This model is qualitatively consistent with *ab initio* calculations that predict the existence of surface states 0.5 eV above the valence-band maximum [2]. According to our model, the acceptor is deep (0.46 eV) with respect to the bulk valence band but shallow (0.08 eV) with respect to the surface states. Since we are measuring the integrated area of the IR peak, broadening due to electron-phonon coupling should not affect the results. However, we cannot rule out the possibility that some of the decrease in absorbance is due to thermal activation of phonon modes.

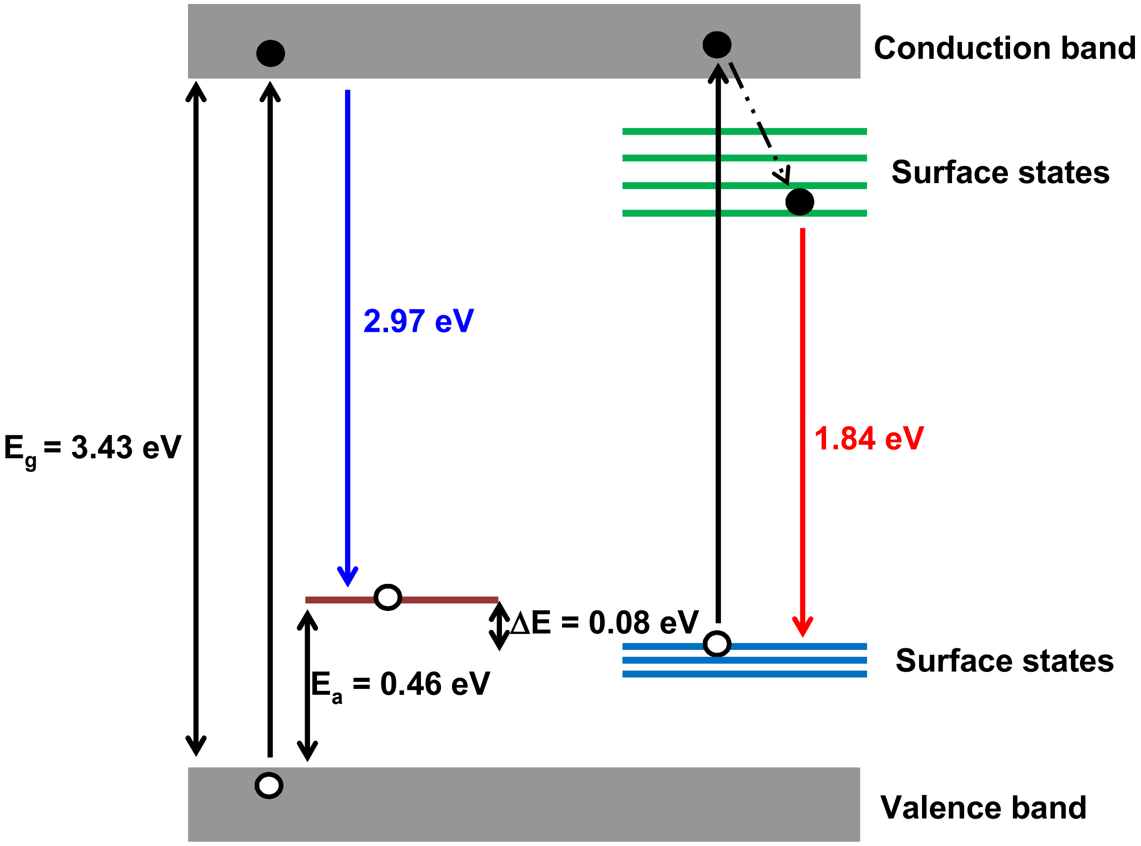

Figure 5.2: Schematic energy-level diagram of ZnO showing the 0.46 eV acceptor level and intragap surface states. Holes are thermally excited to surface states with an activation energy $\Delta E = 0.08$ eV. PL transitions are indicated by vertical downward-pointing arrows.

Figure 5.3 inset shows a low-temperature (10 K) PL emission spectrum at an excitation wavelength of 375 nm (3.31 eV), for the as-grown ZnO nanocrystals. We observed a broad red emission band centered around 675 nm (1.84 eV), similar to the red luminescence observed in ZnO nanowires [3]. By measuring the intensity of the PL as a function of nanowire radius, Shalish *et al.* [3] provided evidence that the red emission originates from surface recombination. In the present work, a photoluminescence excitation (PLE) spectrum (Fig. 5.3) was obtained by measuring the red emission band (at 650 nm) as a function of excitation energy. An onset is observed at 3.0 eV. This feature is consistent with photon energies > 3.0 eV exciting electrons from the surface states to the conduction band. The electrons then fall into surface states in the upper part of the gap and recombine with the holes, resulting in red emission. Photon energies < 3.0 eV excite electrons into the upper surface states, but with a reduced efficiency due to the low density of states.

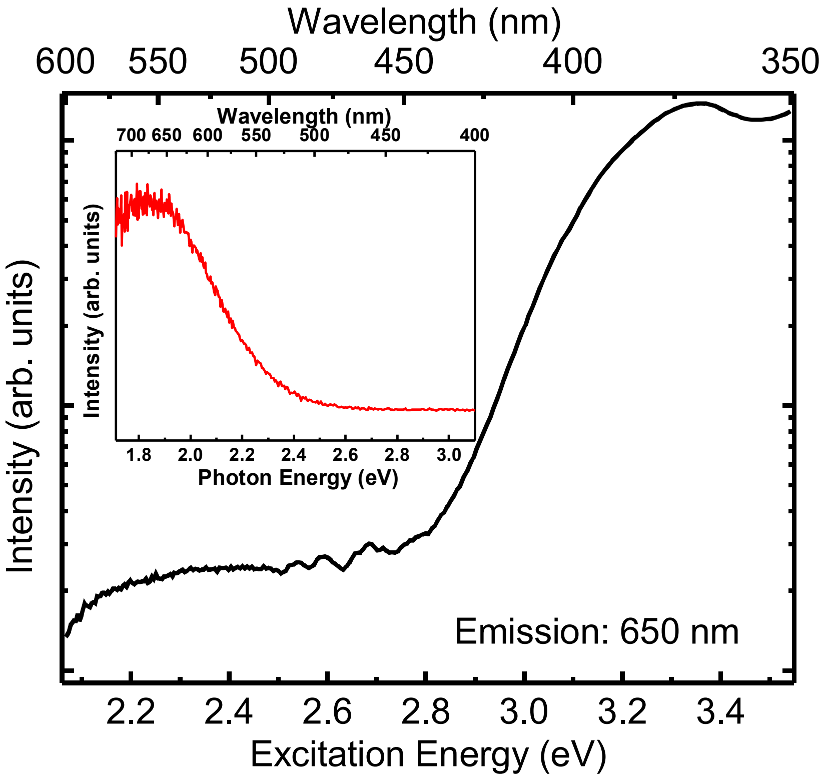

Figure 5.3: Low temperature (10 K) PLE spectrum of ZnO nanocrystals for the red luminescence set at 650 nm wavelength. Inset: Red PL emission (excitation wavelength 375 nm).

In general, surface states may involve defects and impurities. Hydroxides on the surface of ZnO nanocrystals [4], for example, have been correlated with green emission [5]. The previously mentioned surface states, calculated to be 0.5 eV above the valence band, arise from oxygen-deficient surfaces [2]. However, there is also theoretical evidence that the surface states may be intrinsic. Calculations by Kresse *et al.* [6] show that valence-band and conduction-band surface states originate from the $(000\bar{1})$ O-terminated and (0001) Zn-terminated ZnO surfaces, respectively. The surface valence band is quite flat, consistent with our model in Fig. 5.2 [7]. A complete energy-level picture would likely involve a complex mixture of bulk, interface, and surface states.

Figure 5.4 shows a low temperature (10 K) PL spectrum of ZnO nanocrystals under an excitation wavelength of 325 nm. Peaks in the near-band-gap range of 3.18 eV – 3.35 eV have previously been attributed to bound excitons and their phonon replicas. The PL peak at 3.35 eV is due to the neutral donor bound exciton (D^0,X) [8-10]. Low temperature PL peaks at 3.31 eV and 3.22 eV have been attributed to TO and TO+LO phonon replica of donor bound excitons [8, 11]. Fonoberov *et al.* [12] attributed the PL peak around 3.31 eV observed at low temperature ($T < 150$ K) in ZnO nanocrystals to acceptor-bound excitons (A^0,X). They suggested that zinc vacancies or surface defects could act as acceptor impurities. Fallert *et al.* [13] assigned the same PL peak (around 3.31 eV), observed in ZnO powders at 5 K, to excitons bound to defect states at the particle surface. The PL peak at 3.22 eV, recorded at 4.2 K, has been assigned to donor-acceptor pair transitions involving a shallow donor and a shallow acceptor [14]. The emission at 3.26 eV and 3.18 eV could be due to LO phonon replicas of the donor-bound exciton [15].

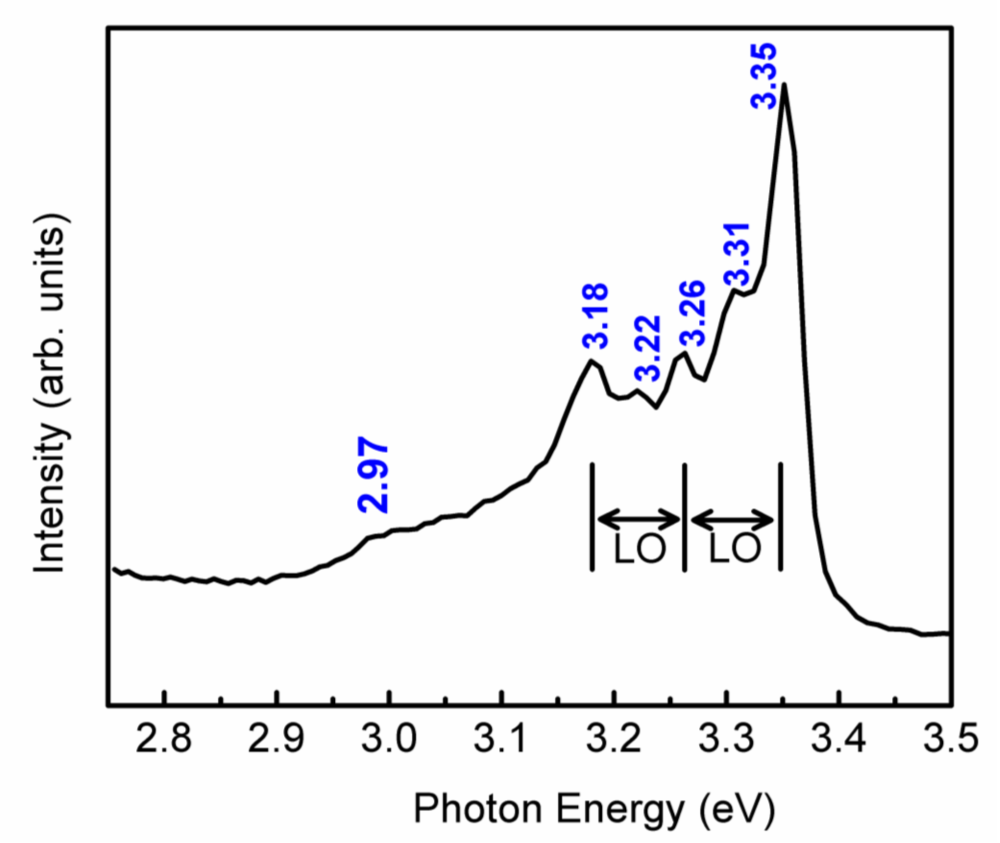

Figure 5.4: Low temperature (10K) PL emission spectrum of ZnO nanocrystals at an excitation wavelength of 325 nm.

We now turn our attention to the emission peak at 2.97 eV. We attribute this peak to the transition of a free electron to the neutral acceptor (Fig. 5.2). In the PL experiment, above-gap light excites electrons into the conduction band. Electrons then fall from the conduction-band minimum to the acceptor level, emitting a photon of energy 3.43 – 0.46 = 2.97 eV. This PL peak supports the argument that ZnO nanocrystals contain acceptors, based on IR and electron paramagnetic resonance measurements [16], with a hole binding energy of 0.46 eV.

5.4 Conclusions

We have studied the defect and surface properties of ZnO nanocrystals, using IR and PL spectroscopy, and developed an energy-level scheme to explain the observations. The measured activation energy (0.08 eV) of the acceptors suggests a band of surface states 0.38 eV above the valence-band maximum, in reasonable agreement with theoretical predictions (0.5 eV) [2]. The presence of surface states also explains the observed red luminescence band centered at 1.84 eV. The PL emission at 2.97 eV is consistent with an acceptor binding energy of 0.46 eV. While 0.46 eV is too deep to achieve bulk *p*-type doping, the low activation energy for exciting holes to the surface states raises the intriguing possibility of *p*-type *surface* conduction.

References

[1]. K. Ozga, T. Kawaharamura, A. Ali Umar, M. Oyama, K. Nouneh, A. Slezak, S. Fujita, M. Piasecki, A. H. Reshak, and I. V. Kityk, Nanotechnology **19,** 185709 (2008).

[2]. J. D. Prades, A. Cirera, J. R. Morante, and A. Cornet, Thin Solid Films **515,** 8670 (2007).

[3]. I. Shalish, H. Temkin, and V. Narayanamurti, Phys. Rev. B **69,** 245401 (2004).

[4]. H. Zhou, H. Alves, D.M. Hofmann, W. Kriegseis, B.K. Meyer, G. Kaczmarczyk, and A. Hoffmann, Appl. Phys. Lett. **80**, 210 (2002).

[5]. N.S. Norberg and D.R. Gamelin, J. Phys. Chem. B **109**, 20810 (2005).

[6]. G. Kresse, O. Dulub, and U. Diebold, Phys. Rev. B **68,** 245409 (2003).

[7]. The calculated surface valence band is slightly below the bulk valence band, in disagreement with our model, which places it 0.38 eV above the bulk valence band.

[8]. T. Matsumoto, H. Kato, K. Miyamoto, M. Sano, E. A. Zhukov, and T. Yao, Appl. Phys. Lett. **81,** 1231 (2002).

[9]. S. W. Kim, S. Fujita, and S. Fujita, Appl. Phys. Lett. **81,** 5036 (2002).

[10]. T. W. Kim, T. Kawazoe, S. Yamazaki, J. Lim, T. Yatsui, and M. Ohtsu, Solid State Commun. **127,** 21 (2003).

[11]. Y. Zhang, B. Lin, X. Sun, and Z. Fu, Appl. Phys. Lett. **86,** 131910 (2005).

[12]. V. A. Fonoberov, K. A. Alim, A. A. Balandin, F. Xiu, and J. Liu, Phys. Rev. B **73,** 165317 (2006).

[13]. J. Fallert, R. Hauschild, F. Stelzl, A. Urban, M. Wissinger, H. Zhou, C. Klingshirn, and H. Kalt, J. Appl. Phys. **101,** 073506 (2007).

[14]. K. Thonke, Th. Gruber, N. Teofilov, R. Schönfelder, A. Waag, and R. Sauer, Physica **B 308-310,** 945 (2001).

[15]. X. Wang, S. Yang, X. Yang, D. Liu, Y. Zhang, J. Wang, J. Yin, D. Liu, H. C. Ong, and G. Du J. Cryst. Growth **243,** 13 (2002).

[16]. S. T. Teklemichael, W. M. Hlaing Oo, M. D. McCluskey, E. D. Walter, and D. W. Hoyt, Appl. Phys. Lett. **98,** 232112 (2011).

Chapter 6 Compensation of zinc oxide nanocrystals by adsorption of formic acid (HCOOH)

In previous chapters we provided evidence that ZnO nanocrystals contain hydrogenic acceptors as-grown. Although the identity of the acceptor is not known, EPR results suggested that it is a zinc vacancy related complex [1, 2]. Using infrared (IR) and photoluminescence (PL) measurements, we have developed a unified model for the acceptor and intragap surface states of ZnO nanocrystals. In this chapter, by adsorption of formic acid (HCOOH) on ZnO nanocrystals, we provide further experimental evidence for this model.

6.1 Experimental

ZnO nanocrystals were synthesized using similar methods discussed in the previous chapters. The sample was exposed to HCOOH vapor for 15 minutes at room temperature. IR spectra were obtained with a Bomem DA8 Fourier transform IR spectrometer with a KBr beamsplitter. HgCdTe and InSb detectors were employed for the spectral ranges of 500 - 5000 cm^{-1} and 1800 - 7000 cm^{-1}, respectively. Low temperature (10 K) measurements were performed in an attached closed-cycle liquid-helium cryostat. PL experiments utilized a JY-Horiba FluroLog-3 spectrometer consisting of double-grating excitation and emission monochromators (1200 grooves mm^{-1} grating) and R928P photomultiplier tube (PMT). The PL spectra were obtained with a double monochromator and 450 W xenon CW lamp as an excitation source and an instrumental correction for the wavelength-dependent PMT response, grating efficiencies, and the variation in the output intensity from the lamp. The IR and PL spectral resolutions were 2 cm^{-1} and 1-3 nm, respectively.

6.2 Disappearing peaks: the silver (Ag) paint story

In previous chapters we showed a low temperature (10 K) series of IR absorption peaks, in the energy range of 0.425 - 0.457 eV, for the as-grown ZnO nanocrystals. The peaks are characteristic of a hydrogenic acceptor spectrum with a hole binding energy of 0.46 eV. These peaks were assigned to transitions to excited states originating from the *A* and *B* valence bands. The 0.46 eV acceptor level was also observed in low-temperature PL spectra [3]. In this section I will discuss the story of the Ag paint which caused the disappearance of these peaks and eventually which led us to investigate the effect of HCOOH on ZnO nanoparticles.

The story begins when I was using Ag paint for contacting my sample (ZnO pellet) with the sample holder for IR measurements. We surprisingly observed that this series of IR peaks disappeared when I used Ag paint as a contact. We thought, at the beginning, that electrons from the Ag metal compensate the acceptors. To determine whether the disappearance of the peaks is due to the Ag metal, I deposited pure Ag metal on a ZnO pellet and performed low temperature IR measurements. However, the Ag-deposited sample showed our series of IR peaks. This result surprised us because it was contrary to our initial hypothesis.

We then started thinking that the disappearance of the peaks could be due to the organic solvent (thinner) in the Ag paint. Indeed, this was true. The peaks disappeared when I exposed the sample to the thinner. However, the thinner is composed of several organic solvents. It was necessary to identify the solvent mixture of the thinner. When I looked at the composition of the thinner, it consisted of the organic solvents acetone, ethyl acetate and n-butyl acetate. I exposed the sample to each of these organic solvents independently. The peaks disappeared only when I exposed the sample to n-butyl acetate. In this way, we isolated the organic solvent responsible for the disappearance of the peaks.

It was necessary to further investigate on n-butyl acetate. N-butyl acetate is synthesized using acetic acid. I exposed my sample to acetic acid, which also caused the peaks to disappear. Then we convinced ourselves that the disappearance of the peaks is due to carboxylic acids in general. This led us to choose the simplest carboxylic acid, formic acid (HCOOH). The peaks indeed disappeared when I exposed the sample to HCOOH. Table 6.1 lists the organic liquids used to induce the disappearance of the IR peaks.

Organic liquids	**IR peaks**
Acetone	Remain
Ethyl acetate	Remain
N-butyl acetate	Disappear
Acetic acid	Disappear
Formic acid	Disappear

Table 6.1: List of the organic liquids used to investigate the disappearance of the IR peaks.

Figure 6.1(a) shows an IR transmission spectrum of the acceptor peaks for the as-grown ZnO nanocrystals at 10 K. A quadratic baseline was subtracted from the transmission spectrum. The peaks disappear when the sample is exposed to HCOOH vapor [Fig. 6.1(b)]. This observation is consistent with our claim that the peaks are due to neutral acceptors. We propose that HCOOH gives electrons to the nanoparticles and thus compensates the observed acceptors. It has been reported that formate species serve as effective electron donors (hole scavengers) on ZnO quantum dots [4]. Studies have shown that HCOOH can be adsorbed dissociatively on the ZnO surface at room temperature, resulting in a formate anion ($HCOO^-$) and hydroxyl species [5-7].

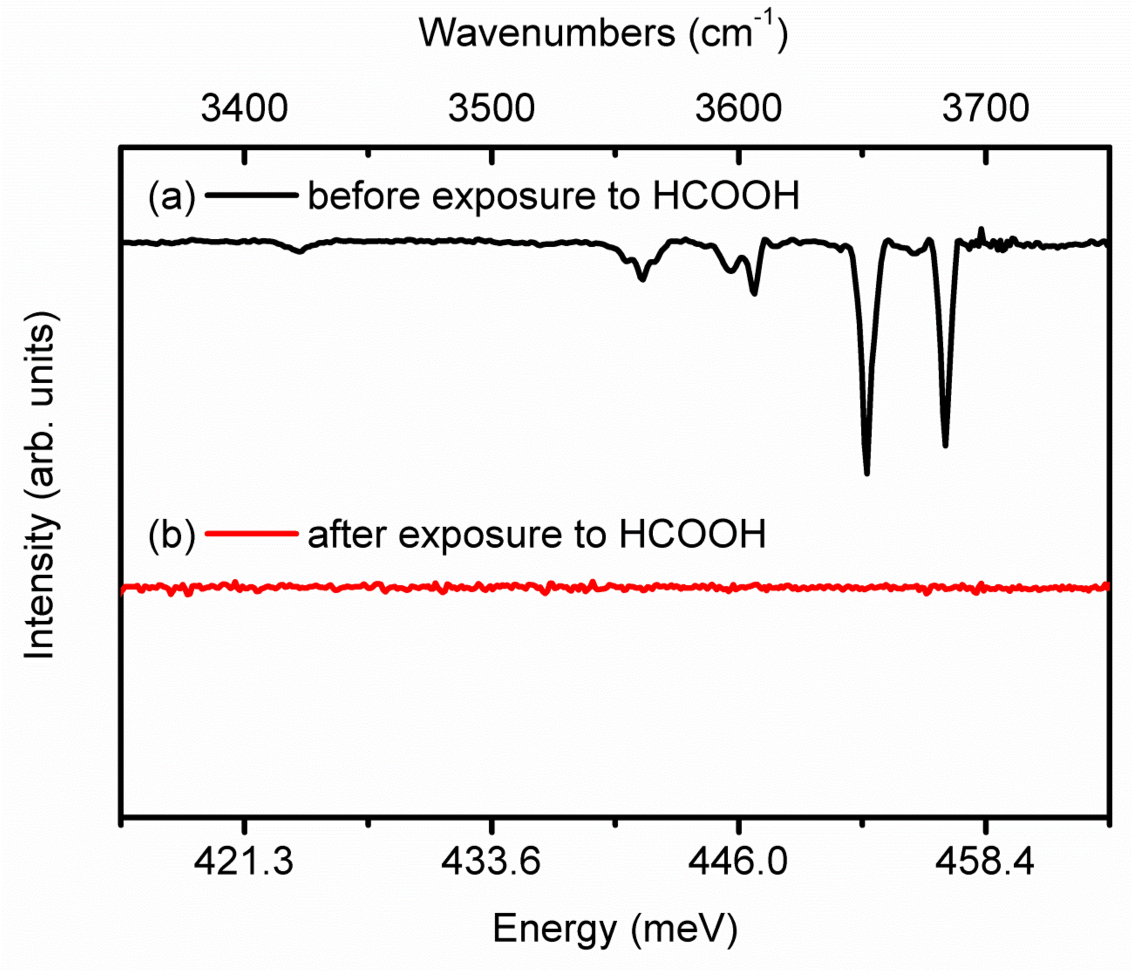

Figure 6.1: Low temperature (10 K) IR transmission spectra of ZnO nanocrystals (a) before and (b) after exposure to formic acid (HCOOH). The disappearance of the peaks indicates compensation of acceptors by formate species. Spectra are shifted vertically for clarity.

6.3 Geometrical structures of the formate anion ($HCOO^-$)

Three geometrical structures (unidentate, bidentate and bridging) have been suggested for the types of coordination of the formate anion, as shown in Fig. 6.2 [5-7]. In ZnO, a surface zinc ion interacts equally with two oxygen atoms of the formate ion in the bidentate structure, whereas in the unidentate form, it interacts with one oxygen atom. In the bridging structure, two oxygen atoms of the formate ion interact with two zinc ions. The structures can generally be identified based on the comparison of the splitting of the COO symmetric and asymmetric stretch modes (Δ_{as-s}). In general, Δ_{as-s} is larger than 200 cm^{-1} for a unidentate-type structure and smaller than 110 cm^{-1} for a bidentate-type structure. For a bridging-type structure Δ_{as-s} is expected to be between 140 - 200 cm^{-1} [8, 9].

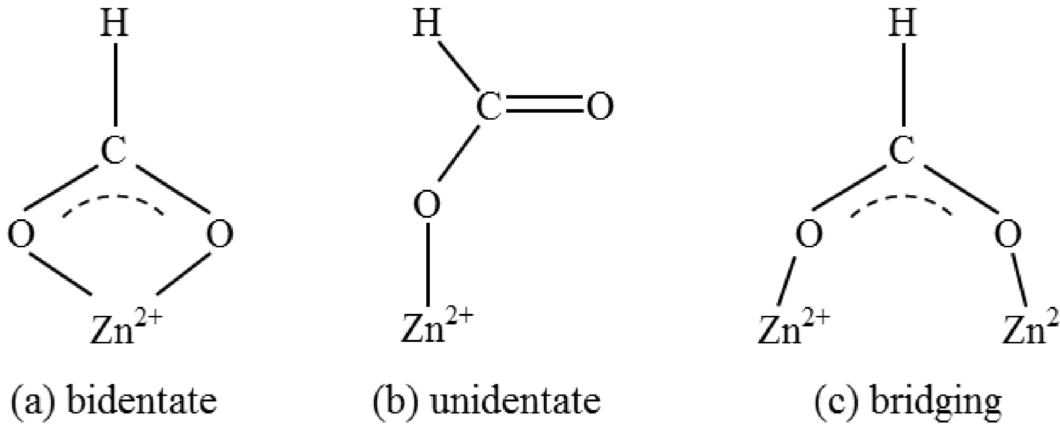

Figure 6.2: Possible geometrical structures for the formate anion on the surface of ZnO.

Using IR spectroscopy, Noto *et al.* [10] have assigned the structure of the formate ion adsorbed on a ZnO surface as bidentate. Crook *et al.*, [11] using high resolution electron energy loss spectroscopy (HREELS), indicated that the formate adopts a bidentate and monodentate-type configuration on the $(10\bar{1}0)$ and $(000\bar{1})$-O surfaces, respectively. Theoretical studies (*ab initio* calculations) on the ZnO $(10\bar{1}0)$ surface suggest that bridging represents the most stable adsorption mode [12].

6.4 Adsorption of HCOOH on ZnO

Figure 6.3 shows room temperature IR absorption spectra for our ZnO nanocrystals exposed to formic acid. The IR absorption spectra were calculated using Absorbance = $\log_{10}(I_R/I)$, where I_R and I are the transmission spectra for the as-grown and formic acid exposed samples, respectively. The sample exposed to HCOOH, Fig. 6.3(a), shows two main features of IR formate absorption bands (characteristic for carboxylic groups coordinated to a metal) at 1320 and 1640 cm^{-1}. These peaks are attributed to symmetric ν_s(COO$^-$) and asymmetric ν_{as}(COO$^-$) stretch modes, respectively [8]. The magnitude of the splitting of their frequencies (Δ_{as-s} = 320 cm^{-1}), suggests that the formate structure is unidentate [Fig. 6.2(b)]. The peaks at 2892 and 790 cm^{-1} are assigned to the ν(CH) stretch mode and δ(CO_2^-) bending mode, respectively [13]. In order to confirm the adsorption of formic acid, we investigated the isotope dependence of the IR spectrum. Fig. 6.3(b) shows the absorption spectrum for ZnO nanocrystals after exposure to deuterated formic acid (DCOOD). The peak at 2171 cm^{-1} is assigned to the ν(CD) stretch mode [13]. This peak has the anticipated isotopic frequency shift from the ν(CH) stretch mode. The COO$^-$ bands formed from DCOOD are identical to those formed from HCOOH. The peak at 1023 cm^{-1} has been observed previously [10] and has been assigned to the δ(CD) bending mode [13].

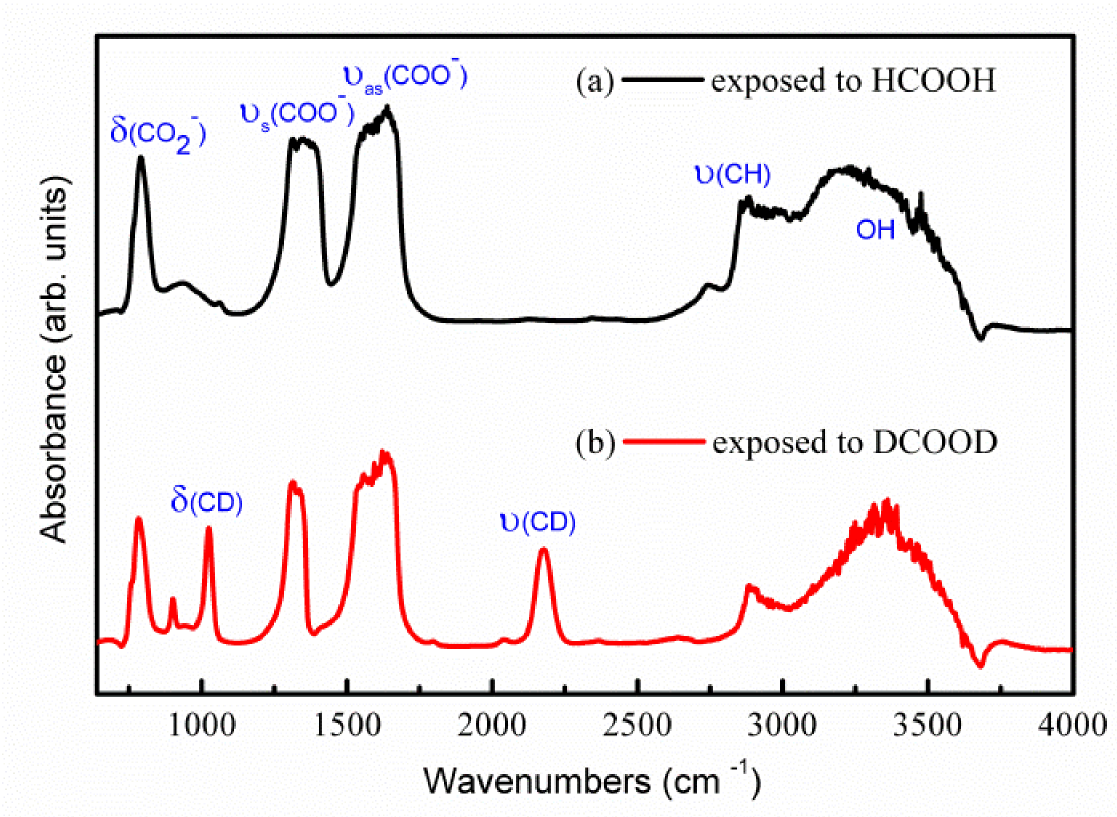

Figure 6.3: Room temperature IR absorption spectra of ZnO nanocrystals after exposure to (a) formic acid (HCOOH) and (b) deuterated formic acid (DCOOD). Spectra are shifted vertically for clarity.

Figure 6.4 shows low temperature (10 K) PL spectra of ZnO nanocrystals, under an excitation wavelength of 325 nm, before and after exposure to HCOOH. Peaks in the near-band-gap range of 3.18-3.35 eV have previously been attributed to bound excitons and their phonon replicas [3]. The emission peak at 2.97 eV was attributed to the transition of free electron to the neutral acceptor. This acceptor peak is no longer evident after exposure to formic acid. Instead, a broad PL emission centered at 3.2 eV appeared [Fig. 6.4(b)]. We attribute this broad peak to an exciton bound to a formate species adsorbed on the surface of ZnO nanocrystals. While the details of this interaction are not known, an increase in the PL intensity after exposure to

HCOOH, in the UV and visible (green) region, has been attributed to surface modifications accompanying formate decomposition [14]. It has also been reported that the green emission [15] correlates with hydroxides on the surface of ZnO nanocrystals [16]. However, the observation of the broad PL emission around 3.2 eV after exposure to HCOOH, to our knowledge, has not been reported previously.

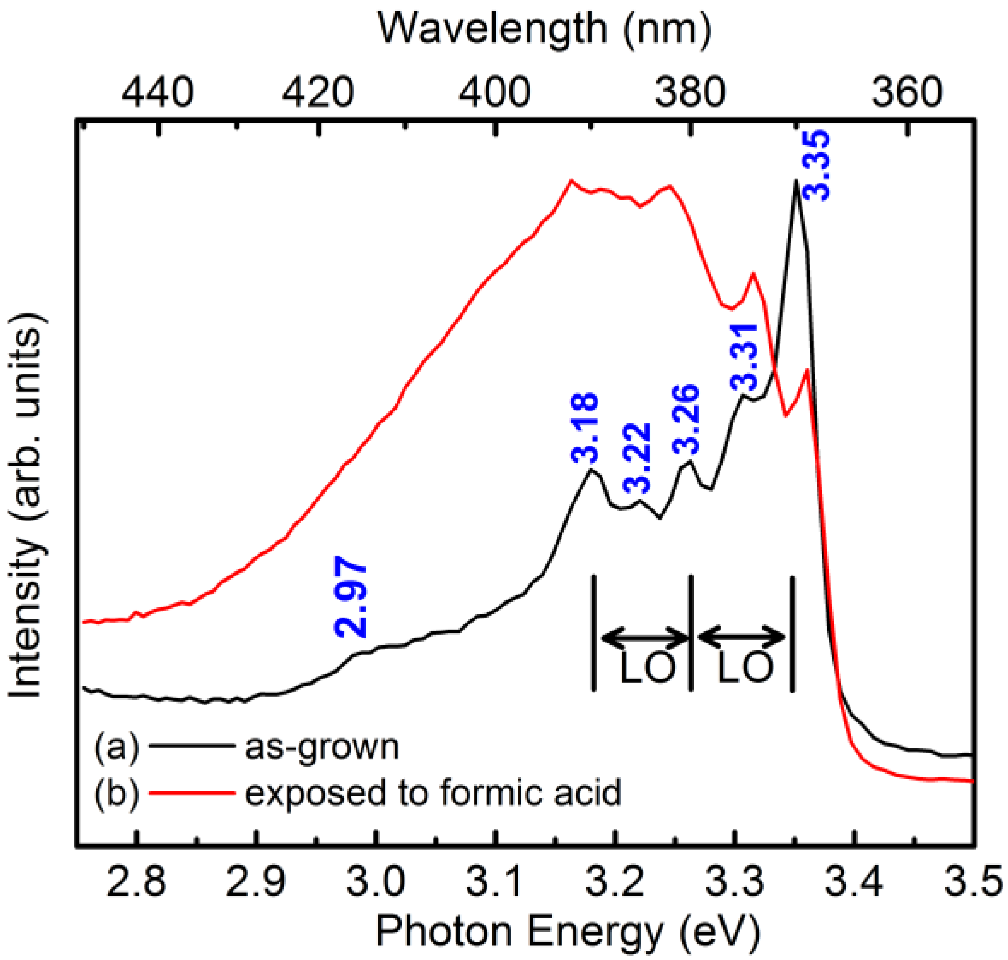

Figure 6.4: Low temperature (10 K) PL emission spectra of ZnO nanocrystals at an excitation wavelength of 325 nm, (a) as-grown and (b) after exposing to HCOOH. The spectra are normalized to the same maximum intensity.

6.4 The concept of redox potential

In this subsection, I will discuss the concept of redox potential, which will help us in understanding the discussion about the energy level of $HCOO^-$ on ZnO (section 6.5).

The redox potential of a substance can be defined as the ease with which the substance loses electrons and becomes oxidized (reducing agent) or gains electrons and becomes reduced (oxidizing agent) [17]. It is a way of quantifying whether a substance is a strong oxidizing agent (has a low electron transfer potential) or strong reducing agent (has a high electron transfer potential). Since the process involves the transfer of electrons, the resulting charge separation can be quantified as a potential difference measured between the ion electrode and a hydrogen electrode under standard conditions. The standard redox potential of hydrogen is zero. The redox potential can also be considered as the affinity of a substance for electrons or its electronegativity compared with hydrogen.

Electron transfer occurs from an occupied quantum state to a vacant state. This can happen when an electronic conductor (metal or semiconductor) is in contact with an electrolyte. In semiconductor physics, the vacuum level has been adopted as a standard reference. Electrochemists express redox potentials on a conventional scale, using the normal hydrogen electrode (NHE) as a reference point. The energy of a redox E, using an absolute scale, is given by

$$E = E_{ref} - eV_{redox}, \tag{6.1}$$

where E_{ref} is the energy of the reference electrode versus the vacuum level (an average value of 4.5 eV for NHE is used) and V_{redox} is the redox potential vs NHE [18-20]. Figure 6.5 shows comparison of the energy scales, the absolute scale (eV) versus electrochemical scale (V). A substance with a negative redox potential donates electrons more readily than a substance with a positive redox potential.

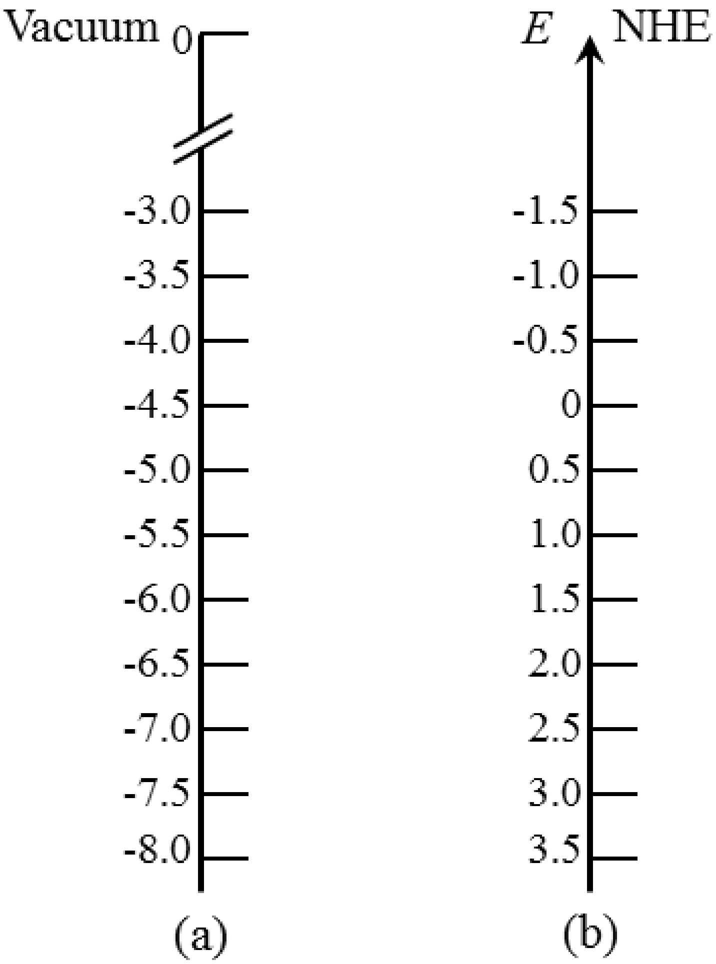

Figure 6.5: Energy scales comparison between (a) absolute scale and (b) electrochemical scale. The references are indicated by the vacuum level and normal hydrogen electrode (NHE) for both scales.

6.5 Energy level of $HCOO^-$ on ZnO

The standard redox potential of $HCOO^-$ in contact with TiO_2 was reported to be 1.9 V vs. NHE [21], or 2.53 V with respect to the conduction-band minimum. Assuming the conduction band edges of ZnO and TiO_2 are roughly the same [22] and taking the band gap of ZnO to be 3.43 eV, one can calculate that the formate ion level is *deep*, ~ 0.9 eV above the valence-band maximum. Fig. 6.6 depicts the energy level diagram of ZnO showing the formate level along with the previously proposed [3] acceptor and intragap surface states. According to this unified model, a band of surface states lies 0.38 eV above the valence-band maximum. We refer to these states as the surface valence band. Similarly, there is a surface conduction band that extends ~ 1 eV into the gap. This model explains the observation of a broad red emission band centered around 675 nm (1.84 eV), which is attributed to surface states [23]. In the present work, exposing the sample to formic acid did not shift the red emission spectrum of ZnO nanocrystals (not shown), consistent with the deep formate level within the gap. The only unoccupied level that can accept an electron from the formate anion is that of the acceptor. All other unoccupied levels are higher than the formate level.

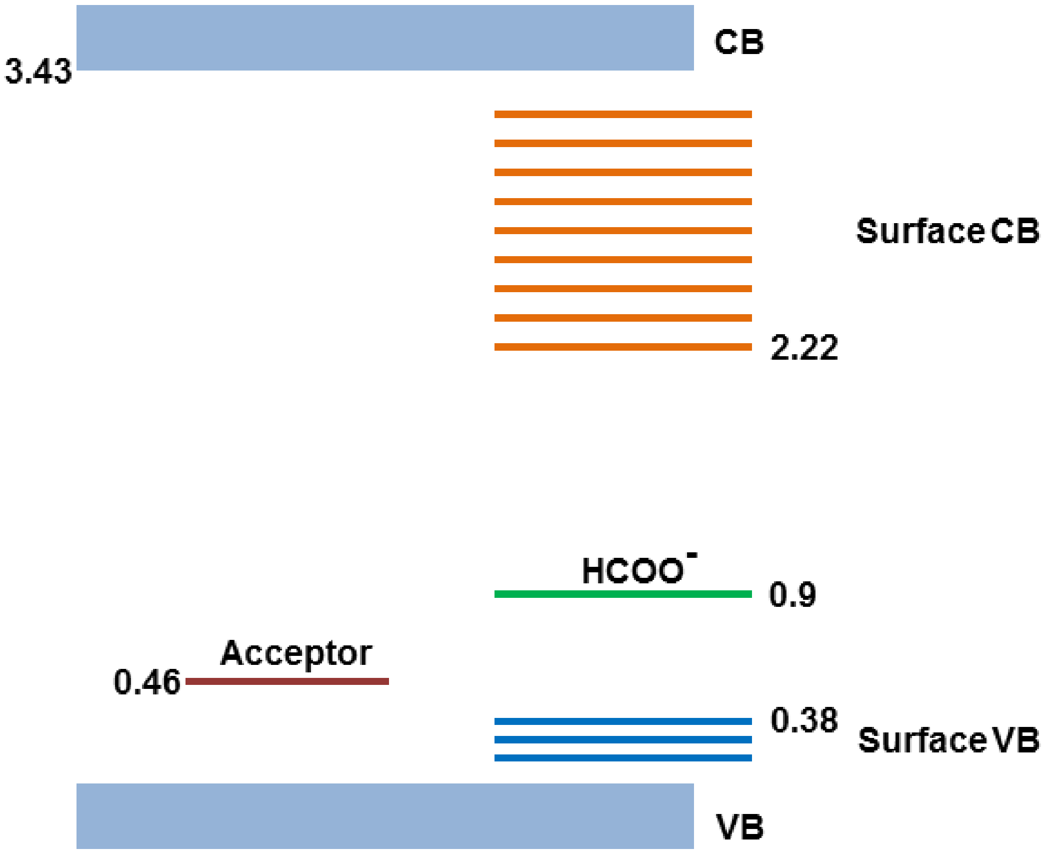

Figure 6.6: Schematic energy-level diagram for ZnO showing the electronic level of the formate ion, with the acceptor level and intragap surface states. Energies are in eV above the valence-band maximum.

6.6 Conclusions

We have presented experimental evidence that confirms the previously observed [24] hydrogenic acceptors on ZnO nanocrystals using IR and PL spectroscopy, and developed and energy-level scheme to explain the observations. After exposure to formic acid, the disappearance of the low temperature IR transition lines indicates that formate ions compensate the acceptors. Room temperature IR measurements show that formic acid is adsorbed on the surface of ZnO nanocrystals as formate species with a unidentate structure. The broad PL emission at 3.2 eV for samples exposed to HCOOH is attributed to an exciton trapped by a surface formate species. The energy level of $HCOO^-$ is estimated to be ~ 0.9 eV above the valence-band maximum.

References

[1]. S. M. Evans, N. C. Giles, L. E. Halliburton, and L. A. Kappers, J. Appl. Phys. **103,** 043710 (2008).

[2]. X. J. Wang, L. S. Vlasenko, S. J Pearton, W. M. Chen, and I. A. Buyanova, J. Phys. D **42,** 175411 (2009).

[3]. S. T. Teklemichael and M. D. McCluskey, Nanotechnology **22,** 475703 (2011).

[4]. E. R. Carraway, A. J. Hoffman, and M. R. Hoffmann, Enoviron. Sci. Technol. **28,** 786 (1994).

[5]. C. T. Au, W. Hirsh, and W. Hirshwald, Surf. Sci. **199,** 507 (1988).

[6]. W. T. Petrie and J. M. Vohs, Surf. Sci. **245,** 315 (1991).

[7]. H. Nakatsuji, M. Yoshimoto, Y. Umemura, S. Takagi and M. Hada, J. Phys. Chem. **100,** 694 (1996).

[8]. A. Lenz, L. Selegård, F. Söderlind, A. Larsson, P. O. Holtz, K. Uvdal, L. Ojamäe, and P.-O. Käll, J. Phys. Chem. C **113,** 17332 (2009).

[9]. K. Nakamato, *Infrared and Raman Spectra of Inorganic and Coordination Compounds*, *Part B, 5th ed*, (Wiley, New York, 1997; p 60).

[10]. Y. Noto, K. Fukuda, T. Onishi and K. Tamaru, Trans. Faraday Soc. **63,** 3081 (1967).

[11]. S. Crook, H. Dhariwal, and G. Thornton, Surf. Sci. **382,** 19 (1997).

[12]. P. Persson and L. Ojamäe, Chem. Phys. Lett. **321,** 302 (2000).

[13]. G. Hussain and N. Sheppard, Spectrochim. Acta, Part A, **43,** 1631 (1987).

[14]. H. Idriss and M. A. Barteau, J. Phys. Chem. **96,** 3382 (1992).

[15]. N. S. Norberg and D. R. Gamelin, J. Phys. Chem. B **109,** 20810 (2005).

[16]. H. Zhou, H. Alves, D. M. Hofmann, W. Kriegseis, B. K. Meyer, G. Kaczmarczyk and A. Hoffman, Appl. Phys. Lett. **80,** 210 (2002).

[17]. R. Baht, A. K. Alias, and G. Paliyath, *Progress in Food Preservation*, (John Wiley and Sons, UK, 2012; p 416).

[18]. H. Gerischer, *Principles of electrochemistry. In the CRC handbook of Solid State Electrochemistry, 1st ed.*, P. J. Gellings and H. J. M. Bouwmeester, Eds. (CRC Press, Inc.: Boca Raton, 1997).

[19]. H. Gerischer, J. Electroanal. Chem. Interfacial Electrochem. **58,** 263 (1975).

[20]. S. Al-Hill and M. Willander, Sensors, **9,** 7445 (2009).

[21]. R. Beranek, B. Neumann, S. Sakthivel, M. Janczarek, T. Dittrich, H. Tributsch, and H. Kisch, Chem. Phys. **339,** 11 (2007).

[22]. N. Serpone, E. Pelizzetti, Eds. *Photocatalysis*: (*Fundamentals and Applications*), (John Wiley and Sons, New York, 1989; p 136).

[23]. I. Shalish, H. Temkin, and V. Narayanamurti, Phys. Rev. B **69,** 245401 (2004).

[24]. S. T. Teklemichael, W. M. Hlaing Oo, M. D. McCluskey, E. D. Walter, and D. W. Hoyt, Appl. Phys. Lett. **98,** 232112 (2011).

Chapter 7 High field electron paramagnetic resonance (EPR) studies of zinc oxide nanocrystals

As we discussed in chapter 4, although the identity of the acceptors in ZnO nanocrystals is not known, EPR results in the X-band (at 9.38 GHz) suggested that it is a zinc vacancy related complex. In this chapter, we further investigated the acceptors with a high field EPR spectrometer in the W-band region. The advantage of using high field EPR spectrometer is that the defect lines can be detected with high resolution, giving rich structural details. We also conducted an EPR experiment with samples exposed to HCOOH to observe the correlation of the disappearance of IR peaks discussed in chapter 6. The experiment was conducted at EMSL, located in PNNL. This work is ongoing research.

7.1 Experimental

A similar procedure described in chapter 4 was used to synthesize ZnO nanoparticles. For this experiment, instead of using sodium hydrogen carbonate ($NaHCO_3$), we used potassium hydrogen carbonate ($KHCO_3$) as a precursor material. The purpose of using $KHCO_3$ precursor is to reduce the Mn EPR lines, observed in the high field, which overlap with the lines of our interest. (The reason why $KHCO_3$ results in less Mn incorporation is not currently understood). In this method, zinc acetate dihydrate [$Zn(CH_3COO)_2 \cdot 2H_2O$] and $KHCO_3$ are reacted at 150 °C for 3 hr in an open-air furnace. The high field EPR spectrometer uses a Varian magnet which has permanent leads (used to energize the coil that produces the magnetic field) and a persistent mode switch, allowing the main field to either be swept or parked at an arbitrary field in the range of 0-9.4 T. The magnet has an internal sweep coil of range +/- 700 G. For cryogenic experiments, the magnet is outfitted with an Oxford continuous flow cryostat. In this work, an operating frequency of 94.8 GHz was used.

7.2 Results and discussion

Figure 7.1 shows low temperature (77 K) high field EPR spectra of ZnO nanocrystals. In the as-grown sample, the measurement showed resonances at $g = 2.003274$, $g = 2.005254$, and $g = 2.007471$ [Fig. 7.1(a)]. The resonances at $g = 2.005254$ and $g = 2.007471$ were not observed in our previous X-band experiment. As discussed in chapter 4, the $g = 2.003$ line is attributed to a hydrogenic acceptor, which may be related to a zinc vacancy complex. In this work, we propose that we have two systems of defects. One has axial symmetry with $g_{\perp} = 2.003274$ and $g_{//} = 2.007471$, and the other is an isotropic line at $g = 2.005254$. We did not observe a complete disappearance of the resonances when the sample is exposed to HCOOH [Fig. 7.1(b)], unlike to the complete disappearance of the IR peaks. Instead, we observed a diminishing intensity of the peaks.

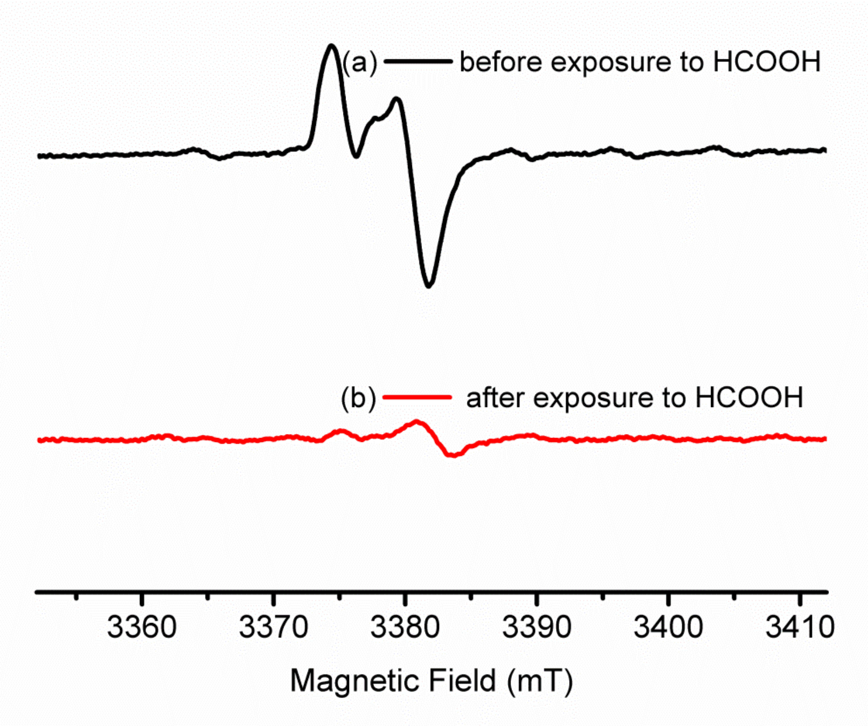

Figure 7.1: High field EPR spectra of ZnO nanocrystals taken at 77 K (a) before and (b) after exposure to formic acid (HCOOH).

Figure 7.2 displays the experimental (black) and fitted (red) high field EPR spectra of ZnO nanocrystals. The data were fitted by numerical simulation of a randomly oriented powder [1]. The Matlab/EasySpin codes are given in Appendix B. Best-fit parameters are listed in Table 7.1.

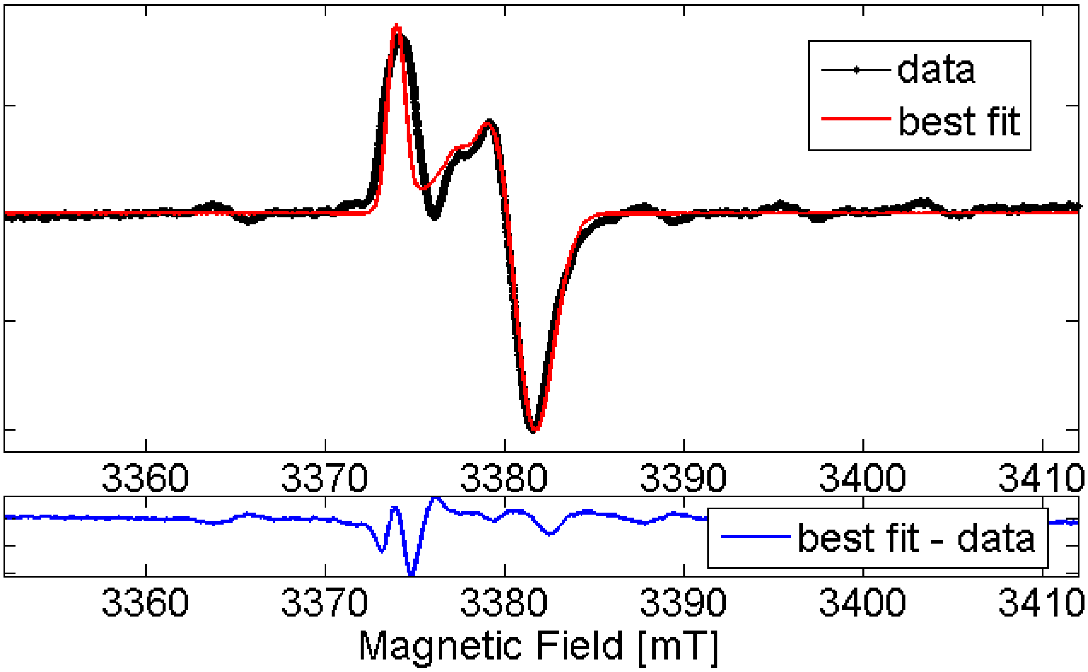

Figure 7.2: Experimental (black) and fitted (red) EPR spectrum of ZnO nanocrystals.

g tensor type		Best-fit parameters
Axial	$g_{\perp}$	2.003274
	$g_{//}$	2.007471
Isotropic	g	2.005254

Table 7.1: EPR best-fit parameters of g value lines after fitting with EasySpin. Notice that the $g_{\perp}$ and $g_{//}$ denote for the axial g tensors which are perpendicular and parallel to the easy axis, respectively. The isotropic g tensor is represented simply by g.

In order to see the consistency of the result, we simulated the W-band spectrum using the observed experimental g parameters and changed the simulation frequency to the X-band. Changing the simulation frequency to X band resulted in isotropic line at $g = 2.004$, which is not in experimental quantitative agreement but it agrees qualitatively. Figure 7.3 shows the simulated spectra of the W and X-bands spectra. The Matlab/EasySpin codes are given in Appendix C.

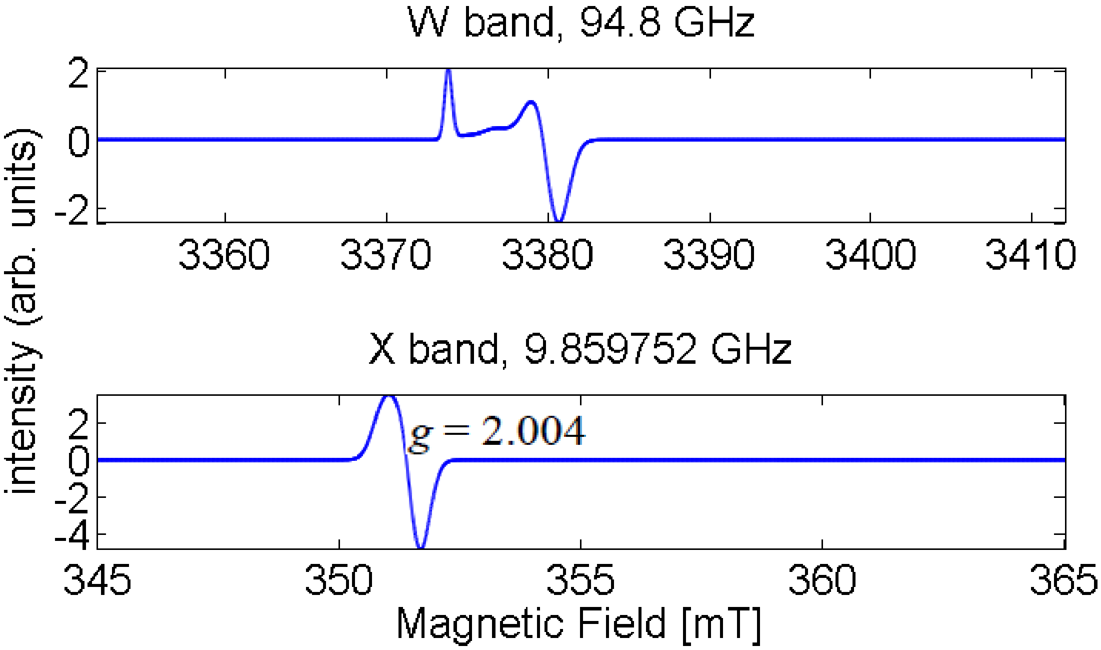

Figure 7.3: Simulated EPR spectra of ZnO nanocrystals in the W and X-bands showing an isotropic line after changing to the simulation frequency to X-band. The X-band simulation which gives a resonance at $g = 2.004$ is not consistent with the experimental EPR spectrum [Fig. 4.4(a)].

7.3 Conclusions

We have performed high field EPR measurements of ZnO nanocrystals, which showed new resonances at $g = 2.005254$ and $g = 2.007471$, in addition to the previously observed line at $g = 2.003274$. We propose a model of two systems with an axial center of $g_{\perp} = 2.003274$ and $g_{//} = 2.007471$ along with an isotropic line at $g = 2.005254$. Samples exposed to HCOOH did not show a complete disappearance of the EPR resonances. Instead, a decrease in intensity is observed.

References

[1]. Stefan Stoll, Arthur Schweiger, J. Magn. Reson. **178(1),** 42-55 (2006).

Chapter 8 Infrared studies of ZnO:Cu nanoparticles

Cu, a common trace impurity in bulk ZnO, has been widely investigated in the past decades due to its interesting optical properties. The frequently observed green emission in ZnO has been attributed due to Cu impurities [1, 2]. In ZnO lattice, Cu sits on a Zn site as Cu^{2+} ($3d^9$) charge state in a tetrahedral coordination and introduces electronic levels into the gap [4]. In the presence of the tetrahedral crystal field, the $3d^9$ energy level is split into the ^2E and $^2T_2$ states. In ZnO, these states are further split due to the trigonal crystal field and spin orbit coupling as shown in Fig. 8.1. At low temperature, the intra-*d* transitions from the lowest sublevel of $^2T_2$ state to two sublevels of the ^2E state give rise to sharp IR absorptions lines at 5782 and 5820 cm^{-1} [4, 5]. The lines $\alpha, \beta, \text{and}\, \gamma$ (zero phonon lines), shown in Fig. 8.1, originate from an intermediately bound exciton of the acceptor type, [$Cu^+(d^9+e)$, *h*]. Under excitation, electrons can be captured by Cu^{2+} (d^9) and a hole is captured by the potential created by this tenth electron forming [$Cu^+(d^9 + e)$, *h*]. The electrons then return to Cu^{2+} state upon green emission [2, 6]. In this section, I will present the concentration dependence of ZnO:Cu nanoparticles by probing the electronic transitions of Cu^{2+} using IR spectroscopy.

8.1 Experimental

Similar synthesis procedure described in chapter 4 was adapted in synthesizing ZnO:Cu nanoparticles. Cu doped zinc acetate precursor was used instead of pure zinc acetate. In this procedure, 12.5 g of $Zn(CH_3COO)_2{\cdot}2H_2O$ was dissolved in 20 ml of water at 80 °C and different amounts of $Cu(CH_3COO)_2$, depending on the concentration needed, were added to the solution (in this experiment 0.01, 0.05 and 0.075 % of $Cu(CH_3COO)_2$ were investigated). The solution was allowed to crystalize by drying overnight. Then using this precursor, ZnO:Cu nanoparticles were grown.

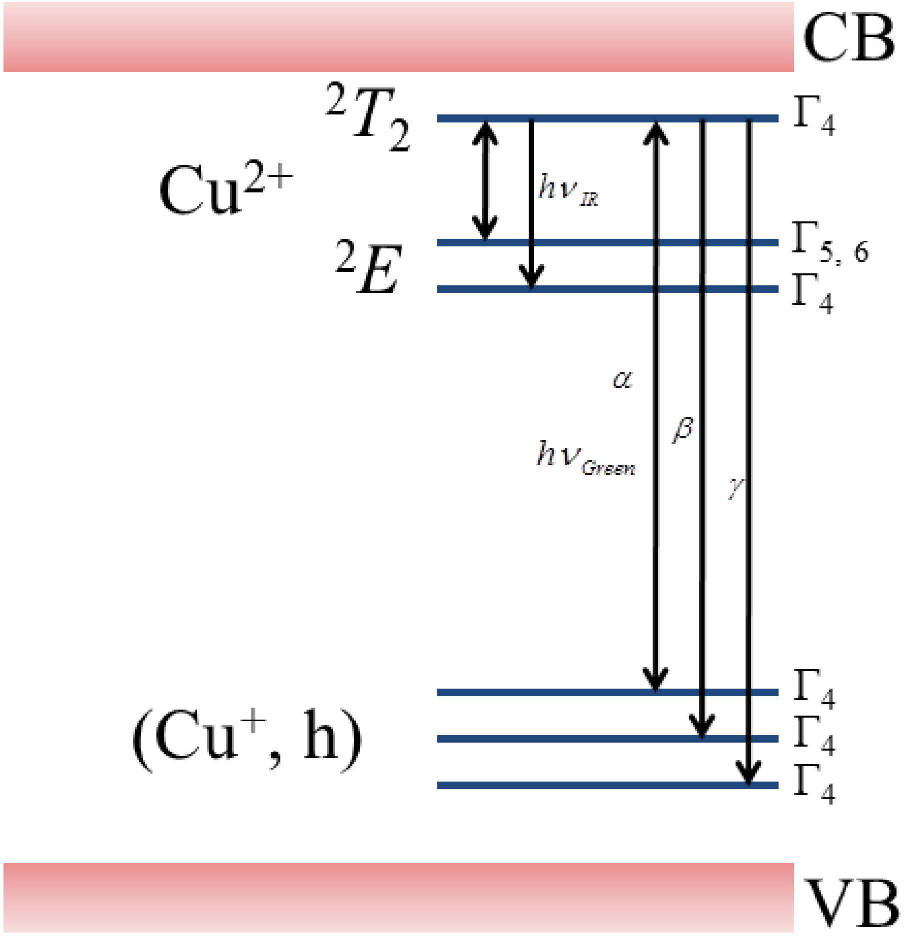

Figure 8.1: Schematic energy-level diagram of Cu in ZnO showing hole transitions which result in IR absorption peaks and green emission. (From Ref. [2].)

8.2 Results and discussion

Figure 8.2 shows Cu concentration dependence of low temperature IR absorption spectra of ZnO:Cu nanoparticles. As shown in the figure, two absorption peaks at energies of 5781 and 5821 cm^{-1} were observed for Cu concentration higher than 0.01%. These absorption peaks arise from the intra-*d* transitions of the Cu^{2+} ion between the lowest sublevel of $^2T_2$ state and two sublevels of the ^2E state, similar to the absorption lines observed in bulk ZnO [4, 5]. However, we have observed a broader width of the absorption peaks in our nanoparticles than the bulk crystals which could be due to inhomogeneous strains and/or electric fields. The as grown series of IR peaks presented in chapter 4 were also observed in the ZnO:Cu nanoparticles (not shown here). However, we found no conclusive evidence that whether the peaks are due to Cu impurities or not.

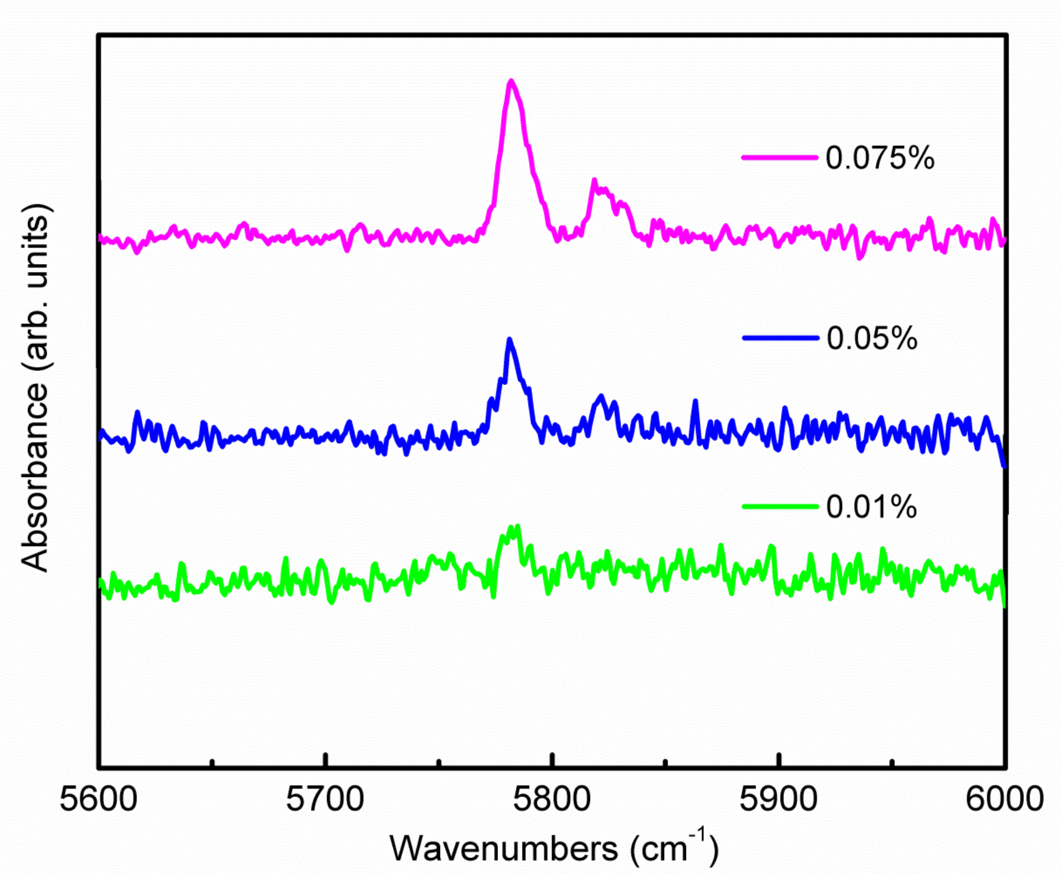

Figure 8.2: Low temperature (10 K) IR absorption spectra of ZnO:Cu, showing dopant concentration dependence of the intra-*d* transitions of Cu^{2+}.

8.3 Conclusions

We investigated dopant concentration dependence of ZnO:Cu nanoparticles, using Cu-doped zinc acetate precursor, by probing the electronic transitions of Cu^{2+}. The intra-*d* transitions of Cu^{2+} ion were observed for Cu dopant higher than 0.01%. The observed transition lines in our nanoparticles showed a broader width of the absorption peaks than in bulk crystals which perhaps is due to inhomogeneous strains and/or electric fields.

References

[1]. R. Dingle, Phys. Rev. Lett. **23,** 579 (1969).

[2]. P. Dahan, V. Fleurov, P. Thurian, R. Heitz, A. Hoffman, and I. Broser, J. Phys.: Condens. Matter **10,** 2007 (1998).

[3]. Y. Kanai, Jpn. J. Appl. Phys., Part 1 **30,** 703 (1991).

[4]. N. Y. Garces, L. Wang, L. Bai, N. C. Giles, L. E. Halliburton, and G. Cantwell, Appl. Phys. Lett. **81,** 622 (2002).

[5]. R. E. Dietz, H. Kamimura, M. D. Struge, and A. Yariv, Phys. Rev. **132,** 1559 (1963).

[6]. G. Xing, G. Xing, M. Li, E. J. Sie, D. Wang, A. Sulistio, Q. L. Ye, C. H. A. Huan, and T. C. Sum, Appl. Phys. Lett. **98,** 102105 (2011).

Chapter 9 Appendices

A. Electric dipole allowed transitions in ZnO

In general, the intensity I of a transition from the state ψ_i to the state ψ_j can be described by

$$I \propto \int \psi_i \mu \psi_j d\upsilon, \tag{A.1}$$

where μ is the transition moment operator and the integration over all coordinates is represented by υ. The type of transition moment we consider here is the electric dipole-allowed transition. For example the transition is said to be x polarized if the integral has a form

$$I_x = \int \psi_i x \psi_j \neq 0. \tag{A.2}$$

Using group theory, one can simply identify which transitions are allowed. The rule is that the direct product representation for the ground and excited states be or contain an irreducible representation to which one or more of the Cartesian coordinates belongs [1]. The ground state is always totally symmetric. Therefore the direct product will in each case be the same as the representations to which the excited state belongs. Equation (A.2) can be written in general form as:

$$I = \left\langle \Gamma_i \middle| \Gamma_{x,y,z} \middle| \Gamma_f \right\rangle \neq 0, \tag{A.3}$$

where Γ_i, Γ_f are irreducible representations for the ground and excited states, respectively. $\Gamma_{x.y,z}$ is the representation of the transition moment for light is polarized along the x, y, or z axis.

As discussed in section 2.2.4, the valence band is composed of p orbitals. For the C_{3v} symmetry such as in ZnO, the p_x and p_y, have Γ_3 representation (two fold degenerate). Light polarized along the x or y axis can excite a transition from the ground state to one of these states. The p_z has Γ_1 representation, which is totally symmetric. Light polarized along the z axis can excite a transition to this state.

Due to the influence of spin-orbit coupling and crystal field, the valence band maximum is split into three bands known as *A*, *B* and *C* states. These states have $\Gamma_4, \Gamma_5 + \Gamma_6$ and Γ_4 symmetries (for C_{3v} point group), respectively. Using group theory arguments and the direct product of the group representations of these band symmetries, we can get the following symmetries.

A state:

$$\Gamma_1 \times \Gamma_4 = \Gamma_4, \tag{A.4}$$

$$\Gamma_3 \times \Gamma_4 = \Gamma_4 + \Gamma_5 + \Gamma_6. \tag{A.5}$$

Similarly for the *B* state:

$$\Gamma_1 \times \Gamma_5 = \Gamma_5,\ \ \Gamma_1 \times \Gamma_6 = \Gamma_6, \tag{A.6}$$

$$\Gamma_3 \times \Gamma_5 = \Gamma_4,\ \ \Gamma_3 \times \Gamma_6 = \Gamma_4. \tag{A.7}$$

where the direct product were found using group multiplication table for the C_{3v} point group symmetry as shown in table A.1.

Therefore applying Equations (A.4) and (A.5) for Equation (A.3), for the *A* state, the possible non-vanishing integrals are:

$$\langle \Gamma_4 | \Gamma_1 | \Gamma_4 \rangle,\ \langle \Gamma_4 | \Gamma_3 | \Gamma_4 \rangle,\ \langle \Gamma_4 | \Gamma_3 | \Gamma_5 \rangle \text{ and } \langle \Gamma_4 \lfloor \Gamma_3 \rfloor \Gamma_6 \rangle. \tag{A.8}$$

Similarly for the B state, the following have non zero integrals.

$$\langle \Gamma_5 | \Gamma_1 | \Gamma_6 \rangle,\ \langle \Gamma_6 | \Gamma_1 | \Gamma_5 \rangle,\ \langle \Gamma_5 | \Gamma_3 | \Gamma_4 \rangle \text{and } \langle \Gamma_6 | \Gamma_3 | \Gamma_4 \rangle. \tag{A.9}$$

Therefore based on the above group theory analysis the allowed hole transition states which originate from the *A* and *B* valence bands are Γ_4, Γ_5 and Γ_6.

$\otimes$	Γ_1	Γ_2	Γ_3	Γ_4	Γ_5	Γ_6
Γ_1	Γ_1	Γ_2	Γ_3	Γ_4	Γ_5	Γ_6
Γ_2	Γ_2	Γ_1	Γ_3	Γ_4	Γ_6	Γ_5
Γ_3	Γ_3	Γ_3	$\Gamma_1 \oplus \Gamma_2 \oplus \Gamma_3$	$\Gamma_4 \oplus \Gamma_5 \oplus \Gamma_6$	Γ_4	Γ_4
Γ_4	Γ_4	Γ_4	$\Gamma_4 \oplus \Gamma_5 \oplus \Gamma_6$	$\Gamma_1 \oplus \Gamma_2 \oplus \Gamma_3$	Γ_3	Γ_3
Γ_5	Γ_5	Γ_6	Γ_4	Γ_3	Γ_2	Γ_1
Γ_6	Γ_6	Γ_5	Γ_4	Γ_3	Γ_1	Γ_2

Table A.1: Group multiplication table for the point group C_{3v}. (From Ref. [2, 3].) (Notice: since an electron spin is considered, we have double groups).

References

[1]. F. A. Cotton, *Chemical Applications of Group Theory*, 3rd ed. (John Wley & Sons, New York, 1990).

[2]. http://www.phyast.pitt.edu/~snoke/resources/resources.html

[3]. G. F. Koster, J. O. Dimmock, R. G. Wheeler, and H. Statz, *Properties of the thirty-two point groups* (MIT Press, Cambridge, 1963).

B. Matlab/EasySpin codes for the high field EPR fitting

```
Sys1.g = [2.0038 2.0076];
Sys2.g = 2.0056;
Sys1.S = 1/2;
Sys2.S = 1/2;
Sys1.gStrain = [0.001 0.0001];
Sys2.gStrain = 0.0009;
Sys1.lw = 0.5;
Sys2.lw = 0.5;
Sys1.weight = 0.9;
Sys2.weight = 0.01;
Vary1.g = [0.00048 0.0018];
Vary2.g = 0.0002;
Vary1.lw = 0.001;
Vary2.lw = 0.001;
Vary1.gStrain = [0.00009 0.00005];
Vary2.gStrain = 0.00001;
Exp.mwFreq = 94.8;     % in GHz
Exp.Range = [3352 3412]; % in mT
Exp.Harmonic = 1;      % first harmonic
Exp.Temperature = 77;  % temperature in Kelvin
Exp.ModAmp = 1;
Exp.Orientations = []; % (an empty array) for powder spectrum
Exp.nPoints = 5460;    % number of point spectrum
[B,spc] = textread('znokhfgcor.txt');
plot(B,spc);
FitOpt.Scaling = 'lsq';
SimOpt.Method = 'perturb';
FitOpt.Method = 'levmar fcn';
esfit('pepper',spc,{Sys1,Sys2},{Vary1,Vary2},Exp,[],FitOpt);
```

```
-- esfit ------------------------------------------------
Simulation function:      pepper
Number of components:     2
Number of parameters:     8
Minimization method:      Levenberg/Marquardt
Residuals computed from:  function as is
Scaling mode:             lsq
Terminated: Parameter step below threshold of 1e-006
---------------------------------------------------------
Best-fit parameters:
    Component 1
          g(1):   2.003274
          g(2):   2.007471
            lw:   0.5007794
    gStrain(1):   0.001649117
    gStrain(2):   0.0004303407
    Component 2
             g:   2.005254
            lw:   0.5000053
       gStrain:   0.0008965738
Residuals of best fit:
    rms  0.0584906
```

```
    mean abs 0.0299569,  max abs  0.420622,  std abs  0.050241
=========================================================
```

C. Matlab/EasySpin codes for the W and X-bands EPR simulation

```
Sys1.g = [2.0038 2.0076];
Sys2.g = 2.0056;
Sys1.S = 1/2;
Sys2.S = 1/2;
Sys1.gStrain = [0.001 0.0001];
Sys2.gStrain = 0.0009;
Sys1.lw = 0.5;
Sys2.lw = 0.5;
Sys1.weight = 0.9;
Sys2.weight = 0.01;
Exp.Harmonic = 1;
Exp.Temperature = 77;
Exp.Orientations = [];
Exp.nPoints = 5460;
Exp.mwFreq = 94.8; Exp.Range = [3352 3412];
[Bw,specW] = pepper({Sys1,Sys2},Exp);
Exp.mwFreq = 9.859752; Exp.Range = [345 365];
[Bx,specX] = pepper({Sys1,Sys2},Exp);
subplot(2,1,1); plot(Bw,specW); axis tight; title('W band, 94.8 GHz');
ylabel('intensity (arb. units)');
subplot(2,1,2); plot(Bx,specX); axis tight; title('X band, 9.859752 GHz');
xlabel('magnetic field [mT]');
ylabel('intensity (arb. units)');
```

D. Electrical properties of ZnO:Al thin film deposition by magnetron sputtering

This work presents the results of a project that was supported by Boeing on the work of ZnO:Al thin film deposition by magnetron sputtering.

Al-doped ZnO thin films have recently attracted resurgent interest and showed a range of applications such as transparent electrodes for photovoltaic devices and flat panel displays [1, 2]. It is stable in hydrogen plasma, which makes it a good candidate in replacing indium tin oxide (ITO) films in amorphous silicon solar cells. ITO films produce a metallic layer in a reducing plasma [3]. Different methods can be used to prepare ZnO:Al thin films such as metal-organic chemical vapor deposition (MOCVD) [4], molecular beam epitaxy (MBE) [5], spray pyrolysis [6], atomic layer deposition (ALD) [7], and magnetron sputtering [8, 9]. Among these techniques, the sputtering process has an advantage due to the requirement of simple apparatus, high deposition rate, and low substrate temperature. In this work the film deposition was performed at Washington State University, Center for Materials Research (CMR).

D1. Experimental

ZnO:Al films were deposited over a 3 inch diameter and 0.7 mm thick of borofloat glass substrate using a BOC Edwards Auto 306 Sputter System. The glass substrates were cleaned using acetone (ACE) and isopropanol (IPA) and dried in a flowing nitrogen gas before they were introduced into the vacuum chamber. The sputtering target used in this experiment was $ZnO:Al_2O_3$. Prior to the deposition, the chamber was pumped down overnight and reached a base pressure of $1.2 \text{ X } 10^{-6}$ Torr. ZnO:Al films were deposited by RF sputtering at a working pressure of 0.03 Torr in an argon atmosphere. The RF power supply was 150 W. A deposition time of 1 hr was used in this experiment. The film thickness was measured using an ellipsometer and was estimated to be 285 nm. The sample was sealed in a quartz ampoule filled with 2/3 atm hydrogen and annealed at 350 °C for 1 hour. Temperature dependent electrical resistivity measurements were performed using a standard 4-probe van der Pauw geometry.

D2. Results and discussion

Figure D.1 shows the temperature dependent resistivity of ZnO:Al film annealed in vacuum, showing a decrease in resistivity upon heating the sample. The sample resistivity at room temperature was 22 Ω.cm and decreased to 0.2 Ω.cm when annealed to 500 K in vacuum. The resistivity of the sample persists upon cooling. When the sample is isochronal air annealed (288 – 500 K), a slight increase in resistivity (from 0.1 to 3.8 Ω.cm) was observed, as shown in Fig. D.2.

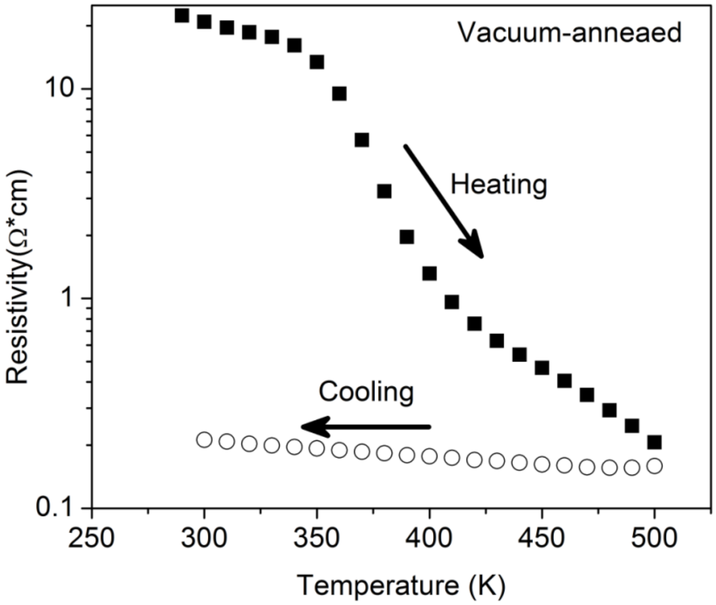

Figure D.1: Temperature-dependent resistivity of ZnO:Al film annealed in vacuum, showing a decrease in resistivity upon heating and recovering the resistivity upon cooling.

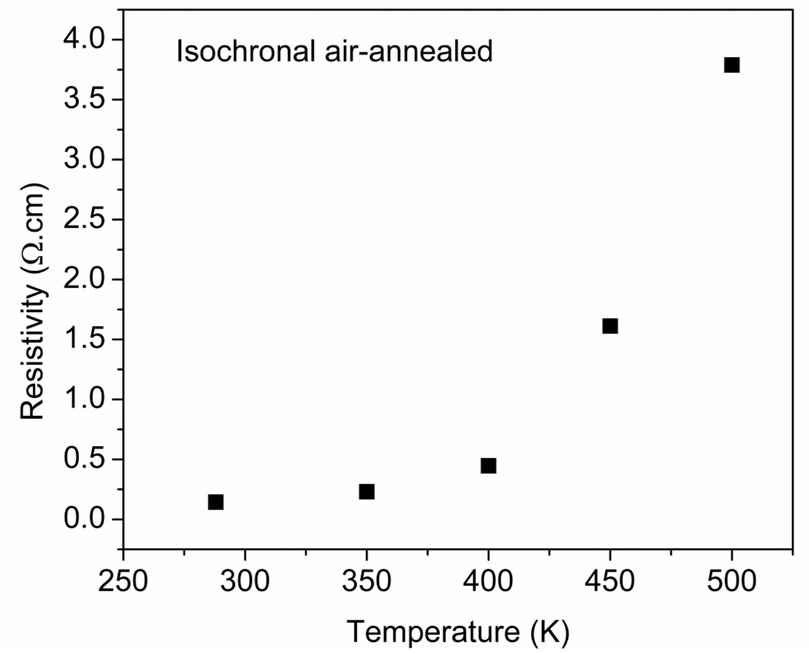

Figure D.2: Temperature-dependent resistivity of ZnO:Al film annealed in air, showing a slight increase in resistivity.

Similar observations by Schmidt *et al.* [10] have been reported on high-resistivity ZnO bulk crystals. They observed that the electrical conductivity of ZnO is strongly influenced by the sample ambient. Annealing under vacuum showed a decrease in resistivity of the sample, due to the presence of conducting electron channel at the surface. This channel is destroyed upon exposure to air. They proposed that the elimination of the surface channel is due to adsorption processes at the surface or a change in surface reconstruction.

Figure D.3 shows the temperature dependent resistivity of ZnO:Al when the sample is annealed in hydrogen at 350 °C for 1 hr prior to vacuum annealing. As shown in the figure, annealing in hydrogen caused the resistivity to dramatically decrease, to the order of 10^{-3} Ω.cm, due to an increase in free carrier concentration. It has been previously reported that hydrogen plays an important role in controlling the electrical conductivity of ZnO [11, 12]. The observed decrease in resistivity upon annealing in hydrogen is consistent with previous results on ZnO nanoparticles, attributed to an increase in free carrier concentration [13].

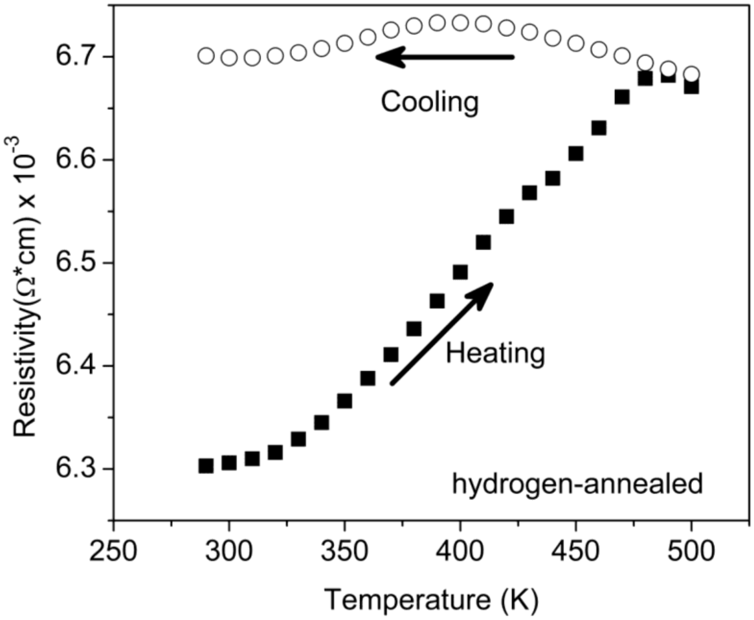

Figure D.3: Temperature-dependent resistivity of ZnO:Al film annealed in hydrogen, showing a dramatic decrease in resistivity (compared to Fig. D.2) due to an increase in free carrier concentration.

D.3 Summary

We have obtained ZnO:Al film on a glass substrate using magnetron sputtering. The observed conductivity of the sample is strongly influenced by the sample ambient. Van der Pauw results showed that vacuum annealing causes the resistivity to decrease with an increase in temperature and persists upon cooling. Air annealing increased the resistivity slightly. Annealing in hydrogen further lowered the resistivity due to an increase in free carrier concentration.

References

[1]. Y. Yamamoto, K. Saito, K. Takakashi, and M. Konagai, Sol. Energy Mater. Sol. Cells **65,** 125 (2001).

[2]. H. S. Bae, M. H. Yoon, J. H. Kim, and Seongil Im, Appl. Phys. Lett. **83,** 5313 (2003).

[3]. S. Major, S. Kumar, M. Bhatnagar, and K. L. Chopra, Appl. Phys. Lett. **49,** 394 (1986).

[4]. B. P. Zhang, K. Wakatsuki, N. T. Binh, N. Usami and Y. Segawa, Thin Solid Films **449,** 12 (2004).

[5]. N. Izyumskaya, V. Avrutin, W. Schoch, A. El-Shaer, F. Reuß, Th. Gruber, and A. Waag, J. Cryst. Growth **269,** 356 (2004).

[6]. R. Ayouchi, F. Martin, D. Leinen and J. R. Ramos-Barrado, J. Cryst. Growth **247,** 497 (2003).

[7]. A. Yamada, B. Sang, and M. Konagai, Appl. Surf. Sci. **112,** 216 (1997).

[8]. S. Maniv and A. Zangvil, J. Appl. Phys. **49,** 2787 (1978).

[9]. O. Takai, M. Futsuhara, G. Shimiza, G. P. Lungu, and J. Nozue, Thin Solid Films **318,** 117 (1998).

[10]. O. Schmidt, A. Geis, P. Kiesel, C. G. Van de Walle, N. M. Johnson, A. Bakin, A. Waag, and G. H. Döhler, Superlattice and Microstructure **39,** 8 (2006).

[11]. C. G. Van de Walle, Phys. Rev. Lett. **85,** 1012 (2000).

[12]. M. D. McCluskey, S. J. Jokela, K. K. Zhuralev, P. J. Simpson, and K. G. Lynn, Appl. Phys. Lett. **81,** 3807 (2002).

[13]. W. M. Hlaing Oo, M. D. McCluskey, J. Huso, and L. Bergman, J. Appl. Phys. **102**, 043529 (2007).

Chapter 10 List of publications

- M. D. McCluskey, W. M. Hlaing Oo, and S. Teklemichael, "Dopants in nanoscale ZnO," *in Functional Metal-Oxide Nanostructures*, ed. J. Wu, W. Han, A. Janotti, H-C. Kim (*Mater. Res. Soc. Symp. Proc. 1174, Warrendale, PA, 2009*), 1174-V07-03.
- S. T. Teklemichael, W. M. Hlaing Oo, M. D. McCluskey, E. D. Walter, and D. W. Hoyt, "Acceptors in ZnO nanocrystals," *Appl. Phys. Lett*. **98,** 232112 (2011).
- S. T. Teklemichael and M. D. McCluskey, "Acceptor and surface states of ZnO nanocrystals: A unified model," *Nanotechnology* **22,** 475703 (2011).
- G. J. Hanna, S. T. Teklemichael, M. D. McCluskey, L. Bergman, and J. Huso, "Equations of state of ZnO and MgZnO by high pressure x-ray diffraction," *J. Appl. Phys*. **110,** 073511 (2011).
- M. D. McCluskey, M. C. Tarun, and S. T. Teklemichael, "Hydrogen in oxide semiconductors," *J. Mater. Res*., accepted for publication.
- S. T. Teklemichael and M. D. McCluskey, "Compensation of acceptors in ZnO nanocrystals by adsorption of formic acid," submitted for publication.